2018年度博士論文

Degradation Diagnosis of Lithium-Ion Batteries Using dV/dQ Curve Analyses and Single Particle Measurement

(微分曲線解析および単粒子測定法による

リチウムイオン電池の劣化メカニズム解析**)**

September, 2018

Keisuke Ando

Graduate School of Urban Environmental Sciences,

Tokyo Metropolitan University

Contents

Chapter 1. General Introduction

1-1. Lithium-ion battery

Since the commercialization of lithium-ion secondary batteries by Sony in 1991, these batteries have been the leading field for Japanese manufacturers. There is an increasing trend observed in the total number of lithium secondary batteries produced worldwide (Figure 1), with the annual total production amount reaching 1 trillion yen (2008). Such energy-storage devices mounted on mobile phones, laptop computers, digital cameras, music players, electric-assisted bicycles, and electric tools support human lives.

The history of lithium batteries started with lithium primary batteries. In 1973, batteries comprising lithium metal as the negative electrode and fluorinated graphite as the positive electrode were developed. Current mainstream includes batteries comprising manganese dioxide as the positive electrode material. As the energy density of a lithium primary battery is dramatically greater than that of other batteries, it has been produced in larger quantities. Next, the development of a lithium battery that could convert a primary battery into a secondary battery was attempted. However, lithium metal precipitates as dendrites (dendritic crystals) as a result of repeated charge–discharge. With the growth of dendrites, the crystals can pierce the separator, causing an internal short circuit between the positive and negative electrodes. In case this phenomenon occurs, the self-discharge of the battery rapidly progresses, generating self-heat, eventually leading to the ignition of the battery. It difficult to use lithium metal as the negative electrode; hence the development of a lithium-metal secondary

battery has been discontinued. As a result, a secondary battery using a graphite-based material as the negative electrode without lithium metal and $LiCoO_2$ as the positive electrode has been developed.

Lithium-ion batteries use organic electrolytes comprising organic solvents (such as ethylene carbonate (EC) and dimethyl carbonate (DMC)) and lithium salts such as $LiPF_6$, and the potential window of the organic electrolyte solution is wider than that of an aqueous electrolyte solution; hence, a lithium-ion battery exhibits high voltage. Therefore, lithium-ion batteries can be developed via the combination of materials with wider redox potentials than those of a lead storage battery; a nickel cadmium battery; and a nickel hydride battery. Owing to the high operating potential and energy density of the lithium-ion battery (Figure 2), as well as lightweight nature, lithium-ion batteries have considerably contributed to downsizing, weight reduction, and longevity of portable electronic equipment.

Figure 3 shows the schematic diagram of the lithium-ion battery. Lithium-ion batteries function as secondary batteries via the insertion and desolating lithium ions in the positive and negative electrodes. Hence, lithium ions move in an electrolyte comprising a lithium salt and an organic solution, and electrons move in the external circuit.

The reaction is expressed as follows.

$$\text{Positive: } LiCoO_2 \rightleftarrows Li_{1-x}CoO_2 + x\,Li^+ + x\,e^-$$

$$\text{Negative: } 6C + x\,Li^+ + x\,e^- \rightleftarrows Li_xC_6$$

$$\text{Total: } LiCoO_2 + 6C \rightleftarrows Li_{1-x}CoO_2 + Li_xC_6$$

Since the topochemical reaction reversibly progresses as shown above, the

lithium-ion battery exhibits stable cycle performance. The required conditions for lithium-ion batteries are shown as follows:

(1) High energy density and high capacity

(2) High output

(3) High cyclability

(4) High safety

(5) Wide operating temperature range

(6) Cost-effectiveness

On the other hand, the lithium-ion battery is well known to degrade during cycle and storage, caused by three main factors, (1) positive electrode degradation, (2) negative electrode degradation, and (3) solid electrolyte interface (SEI) formation, respectively. The degradation of the positive and negative electrodes is caused by the deactivation of active materials due to changes in the surface structure of particles and the electronic disconnection between the active materials and a conductive carbon network or a current collector. SEI formation probably occurs because side reactions such as the decomposition of the electrolyte solution or the deposition of lithium metal leads to an irreversible form of lithium ion.

1-2. dV/dQ curve analysis

The voltage of the lithium-ion battery calculated from the potential difference between the positive and negative electrodes is shown in Equation 1.

$$\mathrm{Voltage}_{\mathrm{cell}} = \mathrm{Potential}_{\mathrm{positive}} - \mathrm{Potential}_{\mathrm{negative}} \quad (1)$$

The potential of the positive or negative electrode is the energy reflecting the electronic state inherent to these materials. Under a constant electronic state, its potential is also constant. With the gradual change in the electronic state, its potential also gradually changes. In addition, with the rapid change in the electronic state of the electrode due to the structure changes by bonding with lithium, the potential also changes rapidly. The dV/dQ curve, which is obtained by the differentiation of a charge or discharge curve of a lithium-ion battery with respect to capacity, shows a peak and slope depending on the voltage change (potential change) (Figure 4). In 2005, I. Bloom et al. have reported the degradation mechanism of a battery by the comparative analysis of the dV/dQ curves before and after the cycle. Positive and negative electrode materials exhibit peculiar values for the peaks and slopes. The analysis of the dV/dQ curve can aid in the determination of the positive and negative electrode states via the evaluation of the change in peaks and the slopes in the cycle and storage.

1-3. Single-particle measurement

The electrodes used in a lithium-ion battery comprise a mixture electrode comprising active material particles, an organic binder, and carbon-based conductive materials (Figure 5). It is typically necessary to analyze a mixture electrode for

estimating the electrochemical characteristics of active materials. However, the performance of the active materials strongly depends on the mixture composition, electrode thickness, and porosity. Furthermore, the current density, electrode potential distribution, and concentration polarization of Li^+ inside the mixture electrode affect the performance of active materials (Figure 6). Therefore, it is difficult to strictly analyze the electrochemical characteristics inherent to the active material.

Therefore, as a method to evaluate the electrochemical characteristics inherent to the active material, a single-particle measurement, in which a thin Au wire used as a current collector probe is brought into direct contact with active material particles to investigate the electrochemical reaction of one particle, has been developed and employed to evaluate active materials. Figure 7 shows the configuration of the single-particle measurement system, comprising a manipulator for manipulating the microelectrodes, an optical microscope for observing the active material, and a potentio-galvanostat for performing various electrochemical measurements. As can be observed in the SEM image of the tip of the current collector probe (Figure 8), a thin-wire structure of Au is sealed in a glass capillary and polished at the tip. In this measurement method, as the current is extremely small (on the order of nanoamperes), it is possible to eliminate the effect of the IR drop originating from material-specific

resistance and cell resistance. In addition, the potential and current distributions become uniform on the particle surface, and the electrochemical characteristic inherent of the active material can be strictly analyzed.

1-4. Research outline

In this paper, I focused on the differential curve analysis (dV/dQ curve analysis) of the discharge curve for examining the effect of multiple degradation phenomena occurring in lithium-ion batteries. The degradation mechanism of lithium-ion batteries under storage and cycle was analyzed by dV/dQ curve analysis. In addition, the degradation mechanism of the positive electrode, which not only underwent degradation but also improved the battery life performance as suggested from the results obtained from the dV/dQ curve analysis, was analyzed in detail by using a single-particle measurement technique.

In chapter 2, I conducted systematic storage life tests using commercial 18650-type lithium-ion batteries with $Li_{1-x}Mn_2O_4$- and $Li_{1-y}Ni_{0.5}Co_{0.2}Mn_{0.3}O_2$-blended positive electrodes at four temperatures (0°C, 25°C, 45°C, and 60°C, respectively) and six state of charges (SOCs) (i.e., 0%, 40%, 60%, 70%, 80%, and 100%, respectively). I conducted a non-disassemble dV/dQ curve

analysis to understand the cell degradation mechanism. The positive electrode/negative electrode reaction region slipped mainly because of cell capacity fading, which was accelerated by the temperature and SOC.

In Chapter 3, understanding the degradation factors (positive electrode and negative electrode degradation and solid electrolyte interface (SEI) formation) of lithium-ion batteries (LIBs) with a blended positive electrode is crucial to improve their durability because battery drive vehicles typically use LIBs with a blended positive electrode due to advantages of power and cost-effectiveness. I developed a dV/dQ curve analysis adapted for a thorough a dQ/dV curve analysis to elucidate the relationship between cycle test conditions and degradation factors. To compare the aforementioned factors, cycle tests were conducted under different conditions: one charge/discharge rate (C/3), two state-of-charge (SOC) ranges (100%–0% and 100%–70%, respectively), and three temperatures (0°C, 25°C, and 45°C, respectively). Clear differences in the degree of contribution from each degradation factor depending on conditions are observed.

In chapter 4, the effects of structural changes on electrochemical performances of the positive electrode-active materials should be understood to improve the durability of lithium-ion batteries. Here, cycle tests were conducted on a commercial lithium-ion cell using the $LiNi_{0.8}Co_{0.15}Al_{0.05}O_2$ positive electrode. Uncycled cells and cells cycled

400 and 800 times were disassembled to obtain their positive electrodes, which were analyzed by scanning transmission electron microscopy and single-particle measurement. After completing 400 cycles, a NiO-like phase was formed on the outermost surface of the particle. Furthermore, after 800 cycles, a NiO-like structure was also formed inside the particle. The rate performance of each single positive electrode particle that was obtained from the composite positive electrode was investigated to evaluate its exchange current density (i_0) and Li^+ apparent diffusion coefficient (D). The decomposition phase at the outermost surface, which was formed during the initial 400 cycles, was clarified to cause the decrease in the exchange current density both electrochemically and quantitatively and the decomposition phase inside the particle, which was formed from 400 to 800 cycles, caused the decrease in the apparent diffusion coefficient of the particle.

References

[1] .Brissot, M. Rosso, J.-N. Chazalviela, S. Lascaud, Dendritic growth mechanisms in lithium/polymer cells, Journal of Power Sources, 81 (1999) 925–929. DOI: 10.1016/S0378-7753(98)00242-0

[2] 特許第 1989293 号（特公平 4-24831 号）二次電池 優先日 1985/05/10（USP 4,668,595 号ほか）（基本特許）.

[3] Y. Makimura, S. Zheng, Y. Ikuhara, Y. Ukyo, Microstructural observation of $LiNi_{0.8}Co_{0.15}Al_{0.05}O_2$ after charge and discharge by scanning transmission electron microscopy, J. Electrochem. Soc. 159 (2012) A1070–A1073. DOI: 10.1149/2.073207jes

[4] S. Watanabe, M. Kinoshita, T. Hosokawa, K. Morigaki, K. Nakura, Capacity fading of $LiAl_yNi_{1-x-y}Co_xO_2$ cathode for lithium-ion batteries during accelerated calendar and cycle life tests (effect of depth of discharge in charge–discharge cycling on the suppression of the micro-crack generation of $LiAl_yNi_{1-x-y}Co_xO_2$ particle), J. Power Sources. 260 (2014) 50–56. DOI: 10.1016/j.jpowsour.2014.02.103

[5] C. Wang, A.J. Appleby, F.E. Little, Electrochemical study on nano-Sn, $Li_{4.4}Sn$ and $AlSi_{0.1}$ powders used as secondary lithium battery anodes, J. Power Sources. 93 (2001) 174–185. DOI: 10.1016/S0378-7753(00)00576-0

[6] J.H. Ryu, J.W. Kim, Y.-E. Sung, S.M. Oh, Failure Modes of Silicon Powder Negative Electrode in Lithium Secondary Batteries, Electrochemical and Solid-State Letters. 7 (2004) A306–A309. DOI: 10.1149/1.1792242

[7] J. Vetter, P. Novák, M.R. Wagner, C.Veit, K.-C. Möller, J.O. Besenhard, M. Winter, M.W.-Mehrens, C. Vogler, A. Hammouche, Ageing mechanisms in lithium-ion batteries, J. Power Sources. 147 (2005) 269–281. DOI: 10.1016/j.jpowsour.2005.01.006

[8] T. Waldmann, A. Iturrondobeitia, M. Kasper, N. Ghanbari, F. Aguesse, E. Bekaert, L. Daniel, S. Genies, I.J. Gordon, M.W. Loble, E.D. Vito, M.W.-Mehrens, Review—Post-Mortem Analysis of Aged Lithium-Ion Batteries: Disassembly Methodology and Physico-Chemical Analysis Techniques, J. Electrochem. Soc. 163 (2016) A2149–A2164. DOI: 10.1149/2.1211609jes,

[9] Y. Merla, B. Wu, V. Yufit, N.P. Brandon, R.F. Martinez-Botas, G.J. Offer, Novel application of differential thermal voltammetry as an in-depth state-of-health diagnosis method for lithium-ion batteries, J. Power Sources. 307 (2016) 308–319. DOI: 10.1016/j.jpowsour.2015.12.122

[10] V.A. Agubra, J.W. Fergus, The formation and stability of the solid electrolyte interface on the graphite anode, J. Power Sources. 268 (2014) 153–162. DOI: 10.1016/j.jpowsour.2014.06.024

[11] M.C. Smart, B.V. Ratnakumar, Effects of Electrolyte Composition on Lithium Plating in Lithium-Ion Cells, J. Electrochem. Soc. 158 (2011) A379–A389. DOI: 10.1149/1.3544439

[10] B.P. Matadi, , S. Geniès, A. Delaille, C. Chabrol, E.d. Vito, M. Bardet, J.-F. Martin, L. Daniel, Y. Bultel, Irreversible Capacity Loss of Li-Ion Batteries Cycled at Low Temperature Due to an Untypical Layer Hindering Li Diffusion into Graphite Electrode, J. Electrochem. Soc. 164 (2017) A2374–A2389. DOI: 10.1149/2.0491712jes

[12] I. Bloom, A.N. Jansen, D.P. Abraham, K.L. Gering, Differential voltage analyses of high-power, lithium-ion cells 1. Technique and application, J. Power Sources. 139 (2005) 295–303. DOI: 10.1016/j.jpowsour.2004.07.021

[13] C. Liu, Z. G. Neale, G. Cao, Understanding electrochemical potentials of cathode materials in rechargeable batteries, Materials Today, 19 (2016) 109–123. DOI: org/10.1016/j.mattod.2015.10.009

[14] I. Bloom, A.N. Jansen, D.P. Abraham, K.L. Gering, Differential voltage analyses of high-power, lithium-ion cells 1. Technique and application, J. Power Sources, 139 (2005) 295–303. DOI: 10.1016/j.jpowsour.2004.07.021

[15] K. Kanamura, Y. Yamada, K. Annaka, N. Nakata, H. Munakata, Electrochemical Evaluation of Active Materials for Lithium Ion Batteries by One (Single) Particle

Measurement, Electrochemistry, 84 (2016) 759–765. DOI: org/10.5796/electrochemistry.84.759

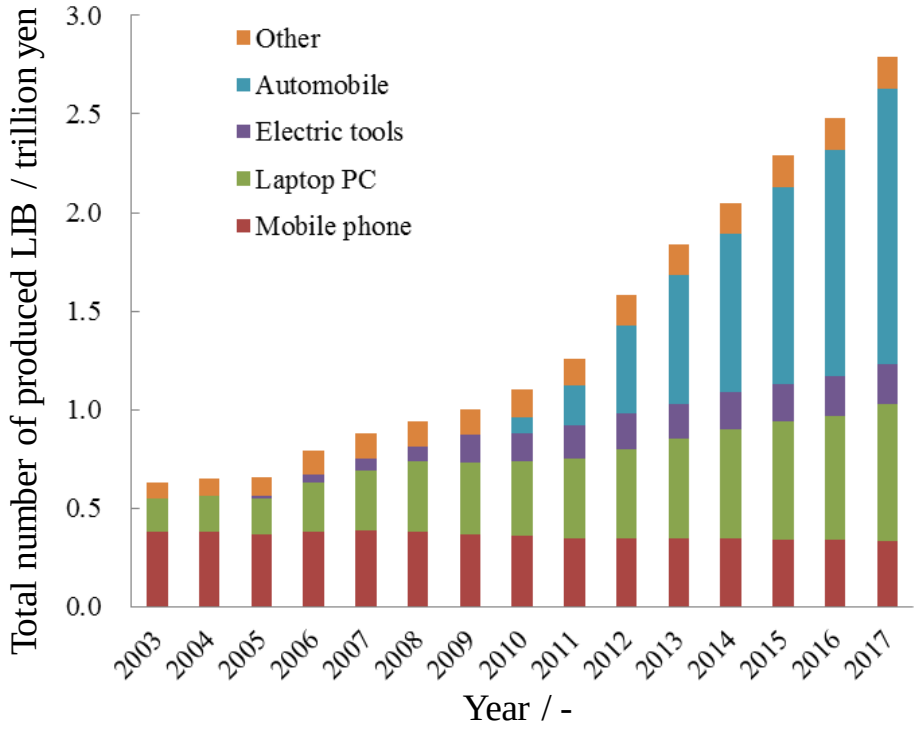

Figure 1. Gross production of lithium-ion batteries.

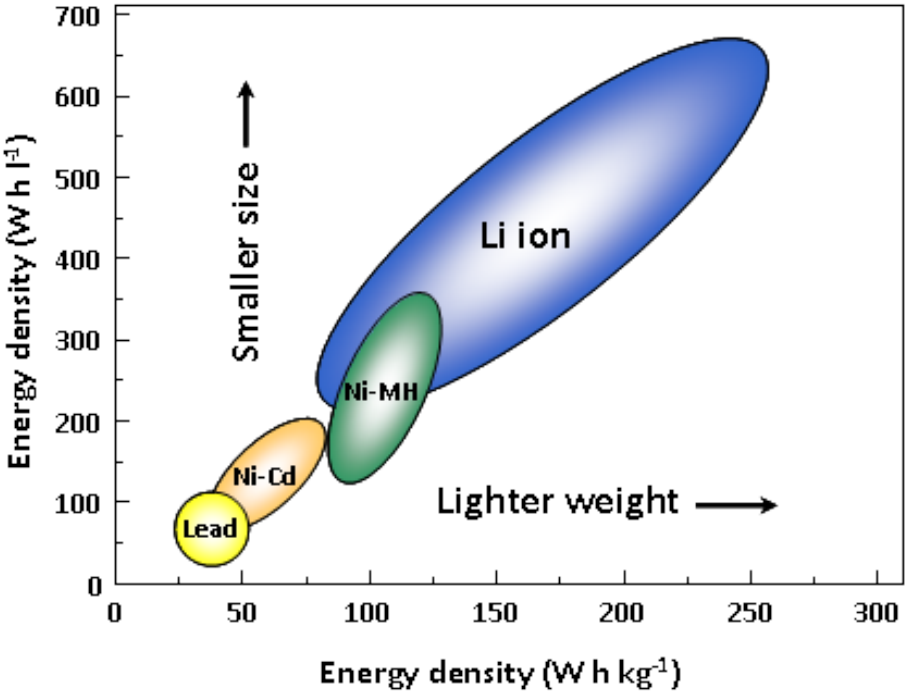

Figure 2. Energy densities of various batteries.

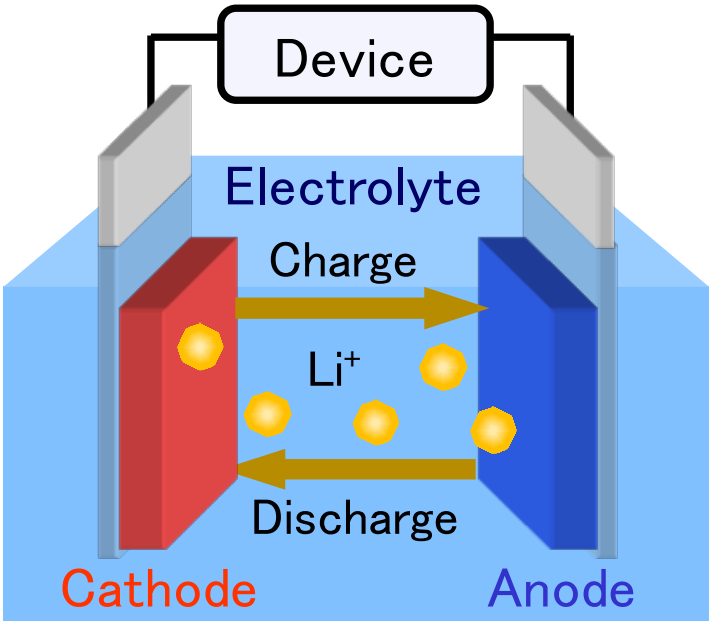

Figure 3. Schematic of a lithium-ion battery using a liquid electrolyte.

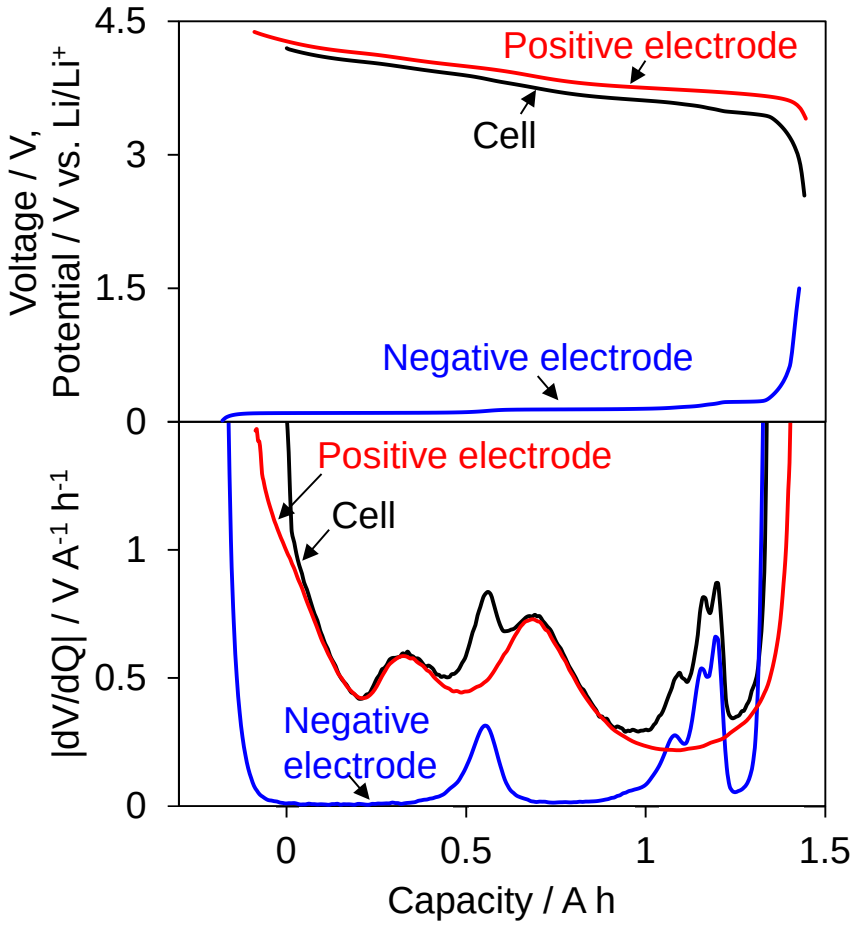

Figure 4. dV/dQ curve of a lithium ion battery and those of the positive and negative electrodes.

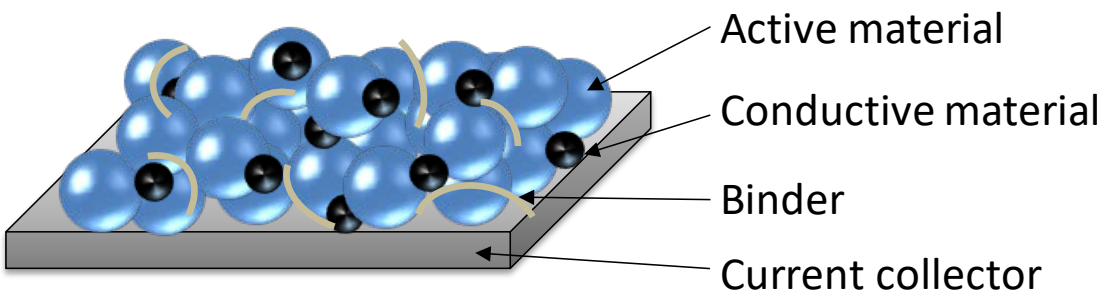

Figure 5. Schematic of a composite electrode.

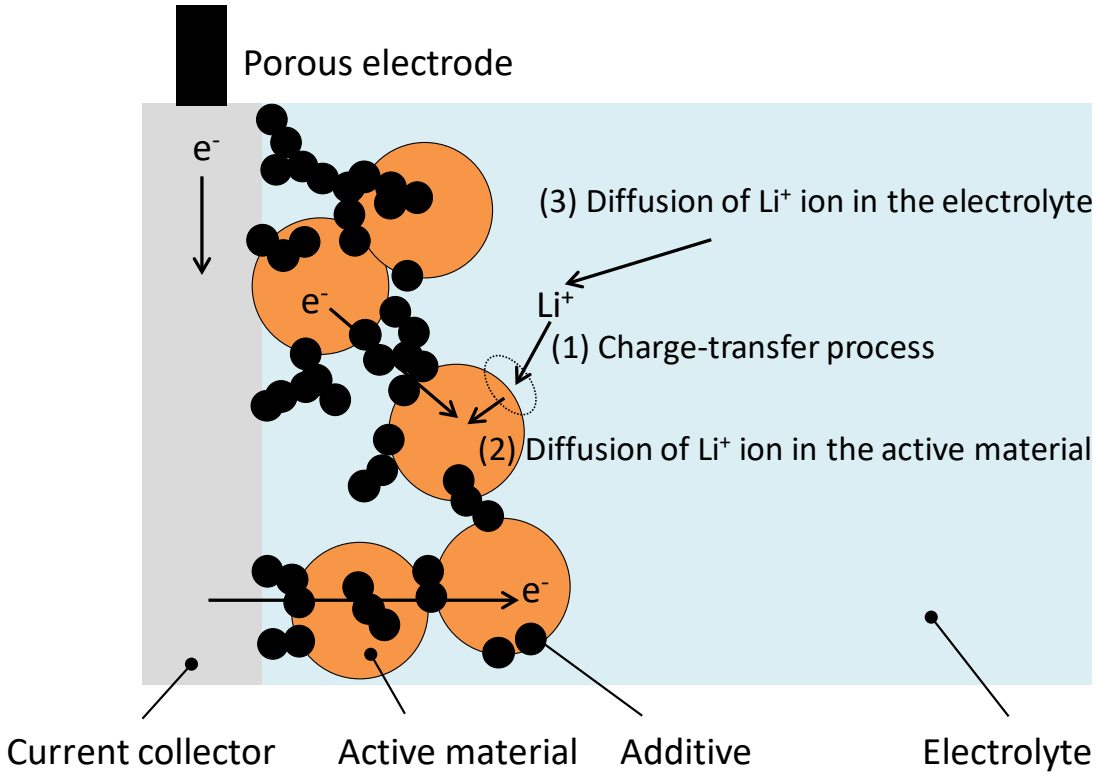

Figure 6. Schematic of the electrochemical processes occurring in a porous electrode.

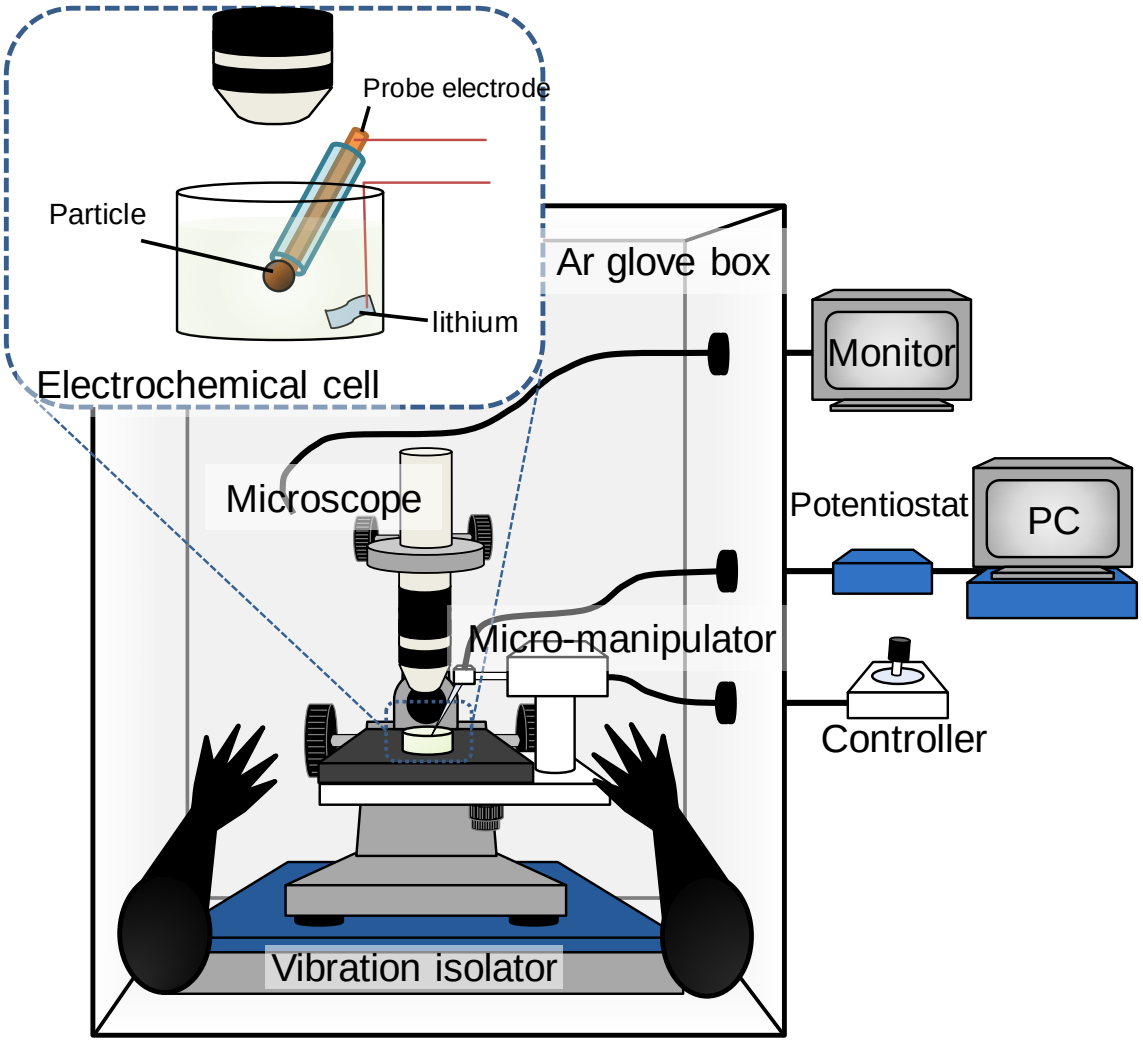

Figure 7. Configuration of a single-particle measurement system.

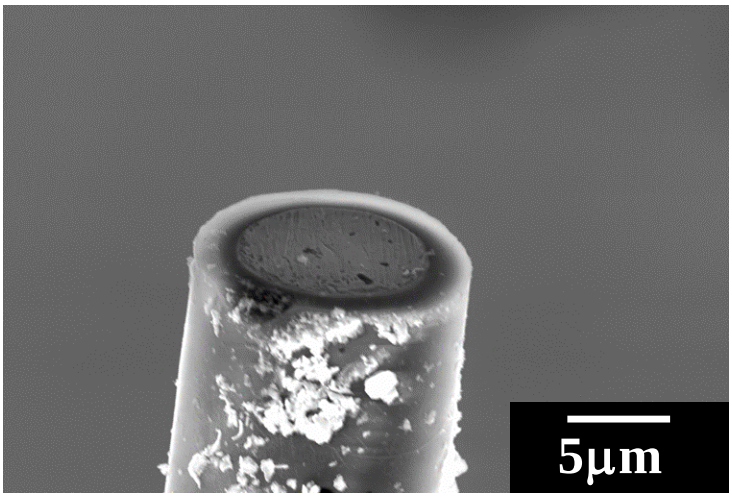

Figure 8. SEM image of the tip of a current collector probe.

Chapter 2.

Calendar Degradation Mechanism of Lithium-Ion Batteries with a $LiMn_2O_4$ and $LiNi_{0.5}Co_{0.2}Mn_{0.3}O_2$ Blended Positive Electrode

2-1. Introduction

Electric vehicles which do not produce polluted gases during driving are coming into wider use due to increasing awareness of environmental problems. Among these vehicles, electric cars equipped with lithium ion batteries are a leading contender, but one issue for broader dissemination is the decrease in driving range due to degradation of lithium ion batteries. The performance of lithium ion batteries (capacity, power) is subject to cycle degradation [1] which occurs due to repeated charging-discharging, and calendar degradation [2] which occurs even if the battery is not used. Vehicles generally spend a longer time parked than driving, and a key issue is improving service life by suppressing the decline in battery performance during parking (calendar degradation).

One known mechanism of calendar degradation of lithium ion batteries is the deactivation of electrochemically active lithium ion which can participate in charging discharging due to side reactions such as decomposition of electrolyte.[3] This mechanism progresses particularly when the battery is stored at a high temperature and

a high state-of-charge (SOC). In addition, when spinel-type lithium manganese oxide ($Li_{1-x}Mn_2O_4$) is used as the positive electrode-active material, degradation occurs by eluting manganese ion into the electrolyte.[4, 5, 6] This degradation progresses particularly when the battery is stored at a high temperature (approx. 45°C or higher) and low SOC (x = 0.1–0.4). Precise understanding of the two degradation factors, which have different SOC susceptibility to degradation, is crucial to improve battery durability.

In recent years, due to advantages of power and cost, practical lithium ion batteries have been realized which use a blended positive electrode of spinel-type lithium manganese oxide and layered rock salt oxide. However, there are few reports on storage life of lithium ion batteries with blended positive electrodes, and almost no cases discussing decomposition of electrolyte at the same time as manganese elution from the positive electrode. This is likely because it is difficult to ascertain the Li composition of each active material based on the cell voltage and SOC in the case of a lithium ion battery with a blended positive electrode.

In this research, the authors conducted storage life test of lithium ion batteries with blended positive electrodes of spinel-type lithium manganese oxide and layered rock salt oxide. The effects of test temperature and SOC on electrolyte decomposition

and elution of manganese from the positive electrode were investigated through analysis of the dV/dQ curve [7, 8] obtained by differentiating the charge-discharge curve, which enables evaluation of degradation in capacity of the positive electrode and negative electrode, and the positive electrode/negative electrode reaction region slips, without disassembling the battery. Here, analysis was conducted regarding the relationship between degradation speed and Li composition of each active material in the blended positive electrode during storage which was calculated from the shape of the dV/dQ curve.

2-2. Experimental

2-2-1. Test battery

The storage life test was carried out using a commercial 18650-type lithium ion battery (positive electrode: blended positive electrode of spinel-type lithium manganese oxide and layered rock salt-oxide type (0.25 $Li_{1-x}Mn_2O_4$, and 0.75 $Li_{1-y}Ni_{0.5}Co_{0.2}Mn_{0.3}O_2$), negative electrode: graphite).

2-2-2. Storage life test conditions

Storage life testing was done under a total of 24 conditions, four conditions for

test temperature (0°C, 25°C, 45°C, 60°C), and six conditions for storage SOC (0%, 40%, 60%, 70%, 80%, 100%). Testing was done with 3 samples (N = 3) for a single condition. For the SOC setting, a battery discharged at a constant current (1C) up to the lower limit voltage (2.50 V) was taken to be 0%, and for 40–100%, charging was done at a constant current (1C) up to each SOC definition voltage indicated in Table 1, and then constant voltage charging was done for 30 minutes or until the current value C/50 was attained. This method is generally called constant current, constant voltage (CCCV) charging. The SOC definition voltages were taken to be the stationary state voltages after first discharging to the lower limit voltage, then charging at 1C until the time when each specified SOC was attained, followed by resting for 6 hours. These SOC adjustments were all carried out at 25°C.

2-2-3. Periodic performance evaluation

In order to compare changes in capacity and internal resistance under each test condition, capacity measurement and DC internal resistance measurement were carried out to evaluate performance at each period shown in Table 2. In capacity measurement, cells were charged to 4.2 V at 25°C with a current value of C/20, then held for 30 minutes or until a current value of C/50 was attained, and finally discharged to 2.75 V

with a current value of C/20. In DC internal resistance measurement, first the SOC was adjusted to 50% (SOC definition voltage: 3.755 V) at 25°C using the method described in the preceding section. Next, charging currents of C/2, 1C, 2C and 3C were applied for 10 seconds each, and resistance was calculated using Ohm's law based on the voltage after 10 seconds. Storage life testing was carried out for a total of approximately 18 months, and as part of that, capacity measurement and DC internal resistance measurement were carried out 8 times, including the initial measurements.

2-3. Results and discussion

2-3-1. Changes in performance due to storage life testing

Figures 1 and 2 show the results of capacity measurement and internal resistance measurement, respectively. First, in terms to temperature dependence, the higher the temperature, the greater the degradation of both capacity and resistance proceeded. Next, in terms of SOC dependence, in storage at 0°C and 25°C, capacity decreased and internal resistance increased with higher SOC. In testing results for 45°C, on the other hand, degradation was accelerated compared to 25°C, and in storage conditions with SOC of 60–70%, there was a marked decrease in capacity and increase in internal resistance. In test results at the highest temperature of 60°C, sudden degradation was

evident at SOCs of 60% and 70% in the initial stage of storage, but as the test period increased, degradation speed slowed down for SOC 70%, and greatest degradation occurred with SOC 60%. The capacity retention rate with SOC 100% decreased at an almost constant rate, and after about 18 months when the test was finished, the capacity retention rate had reached to that of SOC 70% which degraded suddenly at the initial phase of the test. However, the rate of increase in internal resistance for SOC 100% was smaller than SOC 70%. Trends in variation of the rate of increase of internal resistance and variation in the capacity retention rate were the same at 0°C and 25°C, but at 45°C and higher, the degree differed depending on the SOC. In particular, for degradation with an SOC of 60–70%, the rate of increase in internal resistance was high, and the degradation was idiosyncratic.

2-3-2. Differential curve analysis

Analysis of the dV/dQ curve, obtained by differentiating voltage (V) with respect to capacity (Q) in the charge-discharge curve, is known as one technique for evaluating the internal state of a battery[7, 8] Here, the cause of degradation was investigated by applying dV/dQ curve analysis. Figure 3 shows the discharge curve and dV/dQ curve for a battery, prior to the storage life test, obtained via capacity

measurement. Roughly speaking, four peaks were evident in the dV/dQ curve. Based on evaluation of a half-cell with a counter electrode of metallic lithium, using a positive electrode and negative electrode removed by disassembling a battery, the peaks P_1 and P_2 derive from the positive electrode, and peaks N_1 and N_2 derive from the negative electrode. By following changes in the interval between peaks derived from the positive electrode, and the interval between peaks derived from the negative electrode, it is possible to ascertain the degree of degradation of each electrode (Figure 4). In addition, it is possible to estimate the amount of active lithium, due to factors such as decomposition of electrolyte, based on positive electrode/negative electrode reaction region slips. However, with this technique it is not possible to distinguish the active materials in blended positive electrode.

Figures 5–8 show changes in the dV/dQ curve when stored at each temperature. With storage at 0°C (Figure 5), there was no dependence on SOC, and no change was seen in the positive electrode peak interval or negative electrode peak interval, which indicates that no degradation of the electrode-active material was confirmed. As for the peak positions, there were no change in the positive electrode, and the negative electrode peak positions shifted by just the amount of reduction in battery capacity. Hence, the main cause for degradation during storage at 0°C is likely deactivation of

active lithium due to such as decomposition of electrolyte. Just as in storage at 0°C, a shift in the negative electrode peaks was also observed in storage at 25°C (Figure 6), 45°C (Figure 7) and 60°C (Figure 8). On the other hand, with SOC 60% and SOC 70% in storage at 25°C, and with SOC 60%, 70% and 80% in storage at 45°C and 60°C, it was confirmed that peak P_2 derived from the positive electrode shifts to the left, and that there is a narrowing in the interval between peaks P_1 and P_2 derived from the positive electrode. Thus degradation of the positive electrode was confirmed. Degradation of the positive electrode was greater at higher storage temperatures. For this reason, it was found that the idiosyncratic decrease in battery capacity during storage at these SOC was due to degradation of the positive electrode.

The initial battery and batteries stored after 176 days at 60°C were each disassembled, and studied the cause of positive electrode degradations. Figure 9 shows the powder X-ray diffraction patterns of the positive electrode at the atmospheric condition. There was a broadening in the peak near 36.3° at SOC 60% and SOC 70% which is assigned to lithium manganese oxide, suggesting that degradation of lithium manganese oxide of the positive electrode is the cause of decreased capacity. The amount of manganese for the removed negative electrode was measured using inductively coupled plasma mass spectrometry. In the initial battery the amount was

below the detection lower limit, but a large increase of 0.28 μg/mg was seen with SOC 60% and SOC 70%. The reason why internal resistance idiosyncratically increased with these SOC is likely an effect due to positive electrode degradation caused by manganese elution from the lithium manganese oxide, and by SEI covering of the negative electrode surface containing eluted manganese.

2-3-3. Variation in degradation speed

Next, the authors discussed the reasons why the degradation speed suddenly slowed in storage at 60°C and SOC 70%, and why the greatest degradation occurred with SOC 60%. The dV/dQ curve of SOC 70% in Figure 8 (d) shows almost no change in the position of peak P_2 for the positive electrode from 58 days (1st diagnosis) on, and thus it is likely that there was a slowing in manganese elution from lithium manganese oxide.

The ease of manganese elution from lithium manganese oxide ($Li_{1-x}Mn_2O_4$) depends on the Li composition (x value) (6) and thus the x value was investigated during storage life testing with each SOC. As shown in Figure 10, the x value for $Li_{1-x}Mn_2O_4$ during storage was estimated from the charge capacity (SOC adjusted capacity) of CCCV charging to each SOC definition voltage after periodic performance

evaluation, and the dV/dQ curve obtained in the preceding capacity measurement. Taking the fully charged state on the dV/dQ curve to be $x = 1$, and letting peak P_1 be $x = 0.5$ and peak P_2 be $x = 0$, the x value for the SOC adjusted capacity was calculated. Here, in the interval from $x = 1$ to $x = 0$, the reaction of $Li_{1-y}Ni_{0.5}Co_{0.2}Mn_{0.3}O_2$ is small in quantity and almost constant (9), and thus it was assumed that $Li_{1-x}Mn_2O_4$ reacts uniformly. Figure 11 shows the variation in x value at each temperature. For the initial SOC adjustment, the x values of both SOC 60% and 70% are 0.16 and 0.35, respectively, such that manganese elution occurs easily. In case of SOC 70%, the x value exceeds 0.4 in storage at 60°C on the second and subsequent times, and it is difficult for manganese elution to occur. The reason why the x value rises may be because there was a positive electrode/negative electrode reaction region slip due to decomposition of the electrolyte and degradation of the positive electrode-active material, resulting in a rise in charging potential of the negative electrode and positive electrode. On the other hand, the reason why the x value decreased in SOC adjustment on the fourth and subsequent times in SOC 60% storage may be because of the inability to 60% charge due to the increase in internal resistance. The same changes as at 60°C also occurred slowly at 45°C, at test temperatures of 0°C and 25°C the degree of degradation was small, and there was almost no change in the x value.

Regarding the reason why the degradation speed does not slow even from the 5th and subsequent time in SOC 100% storage shown in Figure 1 (d), this is likely because the positive electrode and negative electrode use regions shifted due to decomposition of the electrolyte, thus resulting in increased charging potential of the negative electrode, and a commensurate increase in charging potential of the positive electrode.

2-4. Conclusion

Storage life testing was carried out with temperature and SOC as parameters for lithium ion batteries with a blended positive electrode of spinel-type lithium manganese oxide and layered rock-salt type oxide, and the mechanisms of decreased performance were investigated by analyzing the dV/dQ curve. The results showed that at low temperatures (0°C and 25°C) there was an increase in effective lithium consumption by such as decomposition of electrolyte when SOC was high. At high temperatures (45°C and 60°C) there was an acceleration in degradation with respect to temperature, and there was an idiosyncratic increase in degradation accompanying positive electrode degradation at SOC 60% and SOC 70%. At these SOCs, Li compositions were such that manganese elution occurs easily from lithium manganese oxide in the blended electrode.

Moreover, an increase in the amount of manganese from the negative electrode also supports the idea of manganese elution from the positive electrode. In addition, the slowdown of the degradation at 60°C and SOC 70% suggested that the Li composition of the electrode-active material varies by degradation even if the SOC definition voltage was fixed.

Based on the above results, this research confirmed that there are idiosyncrasies according to the storage conditions, and changes in reactivity due to storage time, in the calendar degradation mechanism of the blended positive electrode lithium ion battery which is affected by manganese elution from the positive electrode dependent on Li composition.

References

[1] T. Matsuda, M. Myojin, K. Ando, D. Imamura, Degradation Analyses of Commercial Lithium-Ion Cells by Temperature/C-rate Controlled Cycle Test, ECS Trans. 64 (2015) 69–75. DOI: 10.1149/06422.0069ecst

[2] M. Ecker, N. Nieto, S. Käbitz, J. Schmalstieg, H. Blanke, A. Warnecke, D.U. Sauer, Calendar and cycle life study of Li(NiMnCo)O_2-based 18650 lithium-ion batteries. J. Power Sources, 248 (2014) 839–851. DOI: 10.1016/j.jpowsour.2013.09.143

[3] V.A. Agubra, J.W. Fergus, The formation and stability of the solid electrolyte interface on the graphite anode, J. Power Sources. 268 (2014) 153–162. DOI: 10.1016/j.jpowsour.2014.06.024

[4] Y. Nishi, Lithium ion secondary batteries; past 10 years and the future. J. Power Sources, 100 (2001) 101–106. DOI: 10.1016/S0378-7753(01)00887-4

[5] N.-S. Choi, J.-T. Yeon, Y.-W. Lee, J.-G. Han, K. T. Lee, S.-S. Kim, Degradation of spinel lithium manganese oxides by low oxidation durability of $LiPF_6$-based electrolyte at 60 °C. Solid State Ionics, 219 (2012) 41–48. DOI: 10.1016/j.ssi.2012.05.012

[6] M. Nishijima, M. Hamano, T. Satio, Y. Nitta, M. Hirayama, and R. Kanno, J. Electrochem. Soc., 163 (9), A1841 (2016).

[7] I. Bloom, A.N. Jansen, D.P. Abraham, K.L. Gering, Differential voltage analyses of high-power, lithium-ion cells 1. Technique and application, J. Power Sources. 139 (2005) 295–303. DOI: 10.1016/j.jpowsour.2004.07.021

[8] K. Honkura, K. Takahashi, T. Horiba, Capacity-fading prediction of lithium-ion batteries based on discharge curves analysis, J. Power Sources. 196 (2011) 10141–10147. DOI: 10.1016/j.jpowsour.2011.08.020

[9] T. Kobayashi, N. Kawasaki, Y. Kobayashi, K. Shono, Y. Mita, H. Miyashiro, A method of separating the capacities of layer and spinel compounds in blended cathode, J. Power Sources. 245 (2014) 1–6. DOI: 10.1149/07523.0077ecst

Table 1. SOC definition voltage.

SOC	**40%**	**60%**	**70%**	**80%**	**100%**
Voltage	3.676 V	3.849 V	3.937 V	4.009 V	4.200 V

Table 2. Test period between diagnoses.

Number of diagnoses	**Initial**	**1st**	**2nd**	**3rd**	**4th**	**5th**	**6th**	**7th**
Test period (days)	0	58	110	165	228	331	430	529

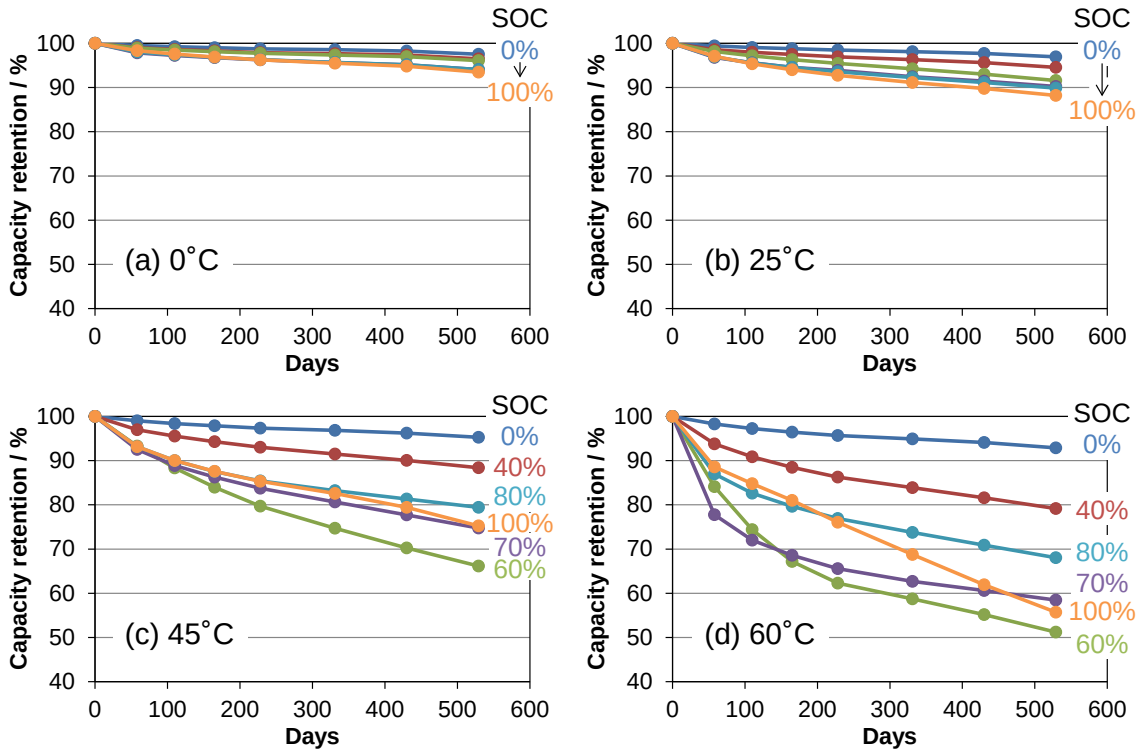

Figure 1. Capacity retentions in storage life tests at (a) 0°C, (b) 25°C, (c) 45°C, and (d) 60°C measured at 25°C with C/20 current rate between 2.75 V and 4.2 V.

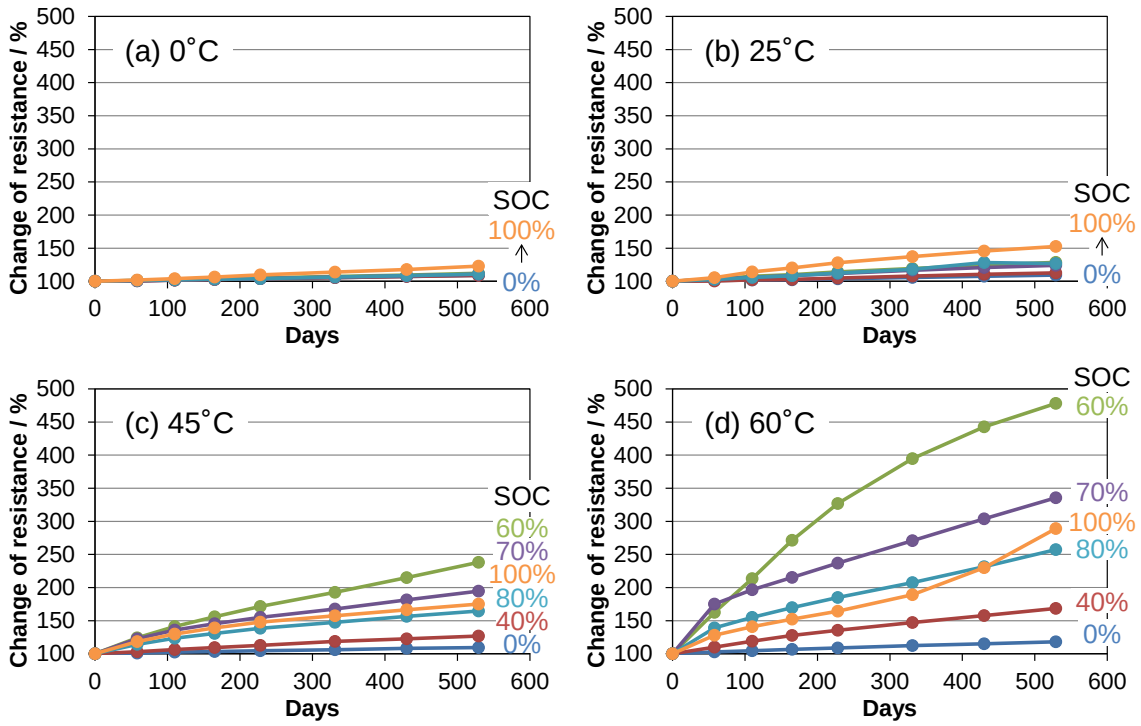

Figure 2. Internal resistance changes in storage life tests at (a) 0°C, (b) 25°C, (c) 45°C, and (d) 60°C measured at 25°C, SOC 50%.

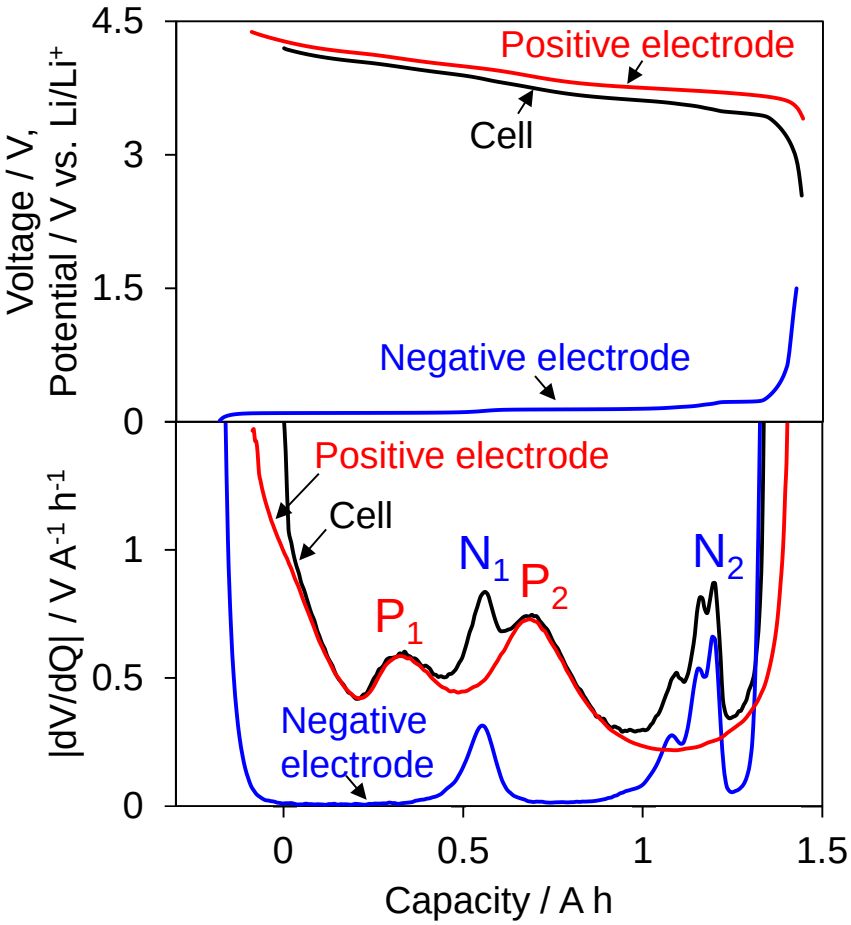

Figure 3. Voltage curves (upper) and dV/dQ curves (lower) of initial state during discharge at C/20. Black, red and blue lines represent cell, positive electrode and negative electrode, respectively.

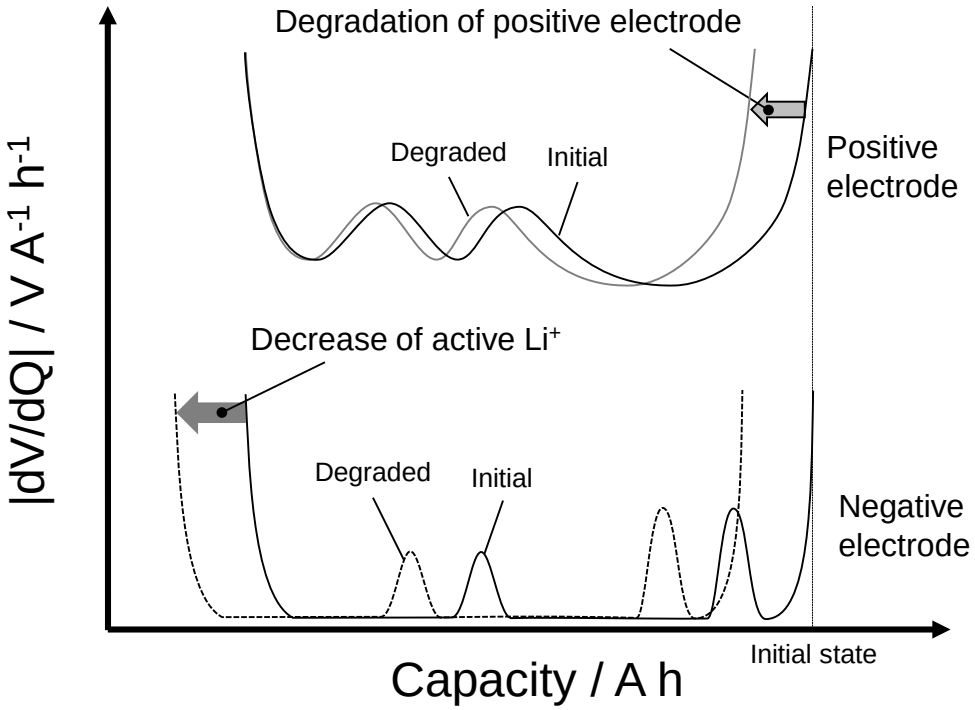

Figure 4. Schematic diagram of capacity decrease factor of lithium ion batteries by dV/dQ curve analysis.

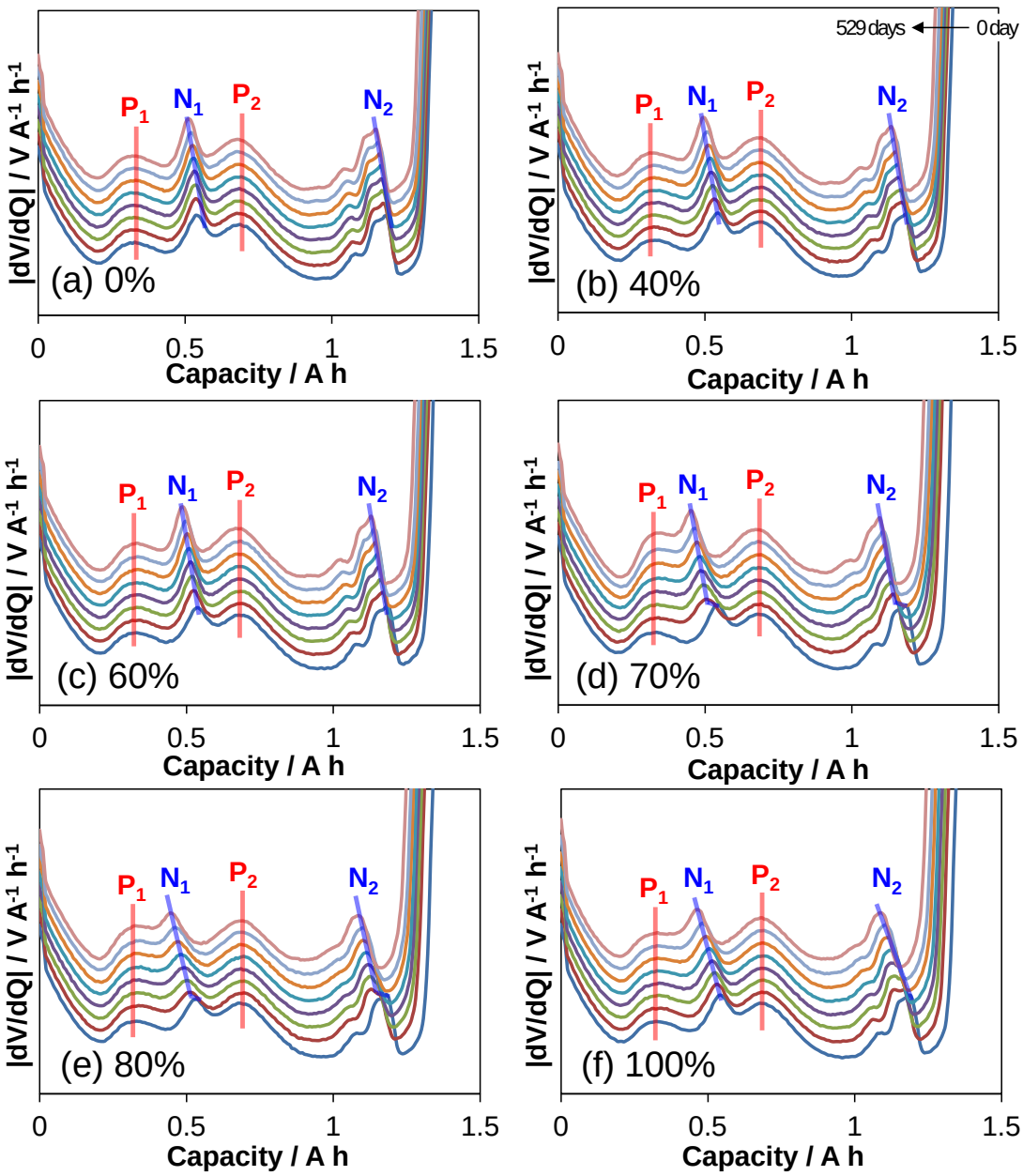

Figure 5. Changes of dV/dQ curve shapes during the storage life tests at 0°C.

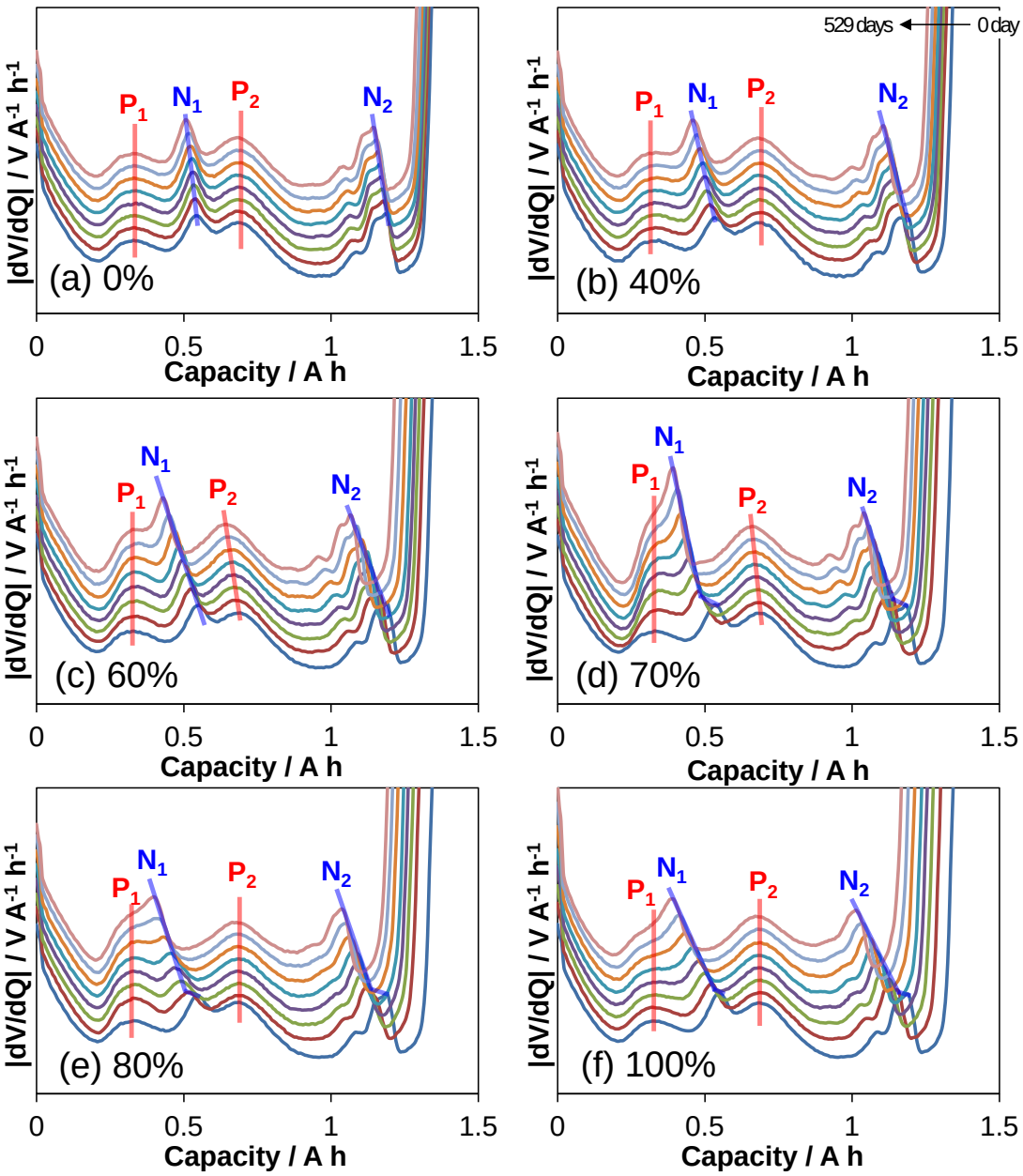

Figure 6. Changes of dV/dQ curve shapes during the storage life tests at 25°C.

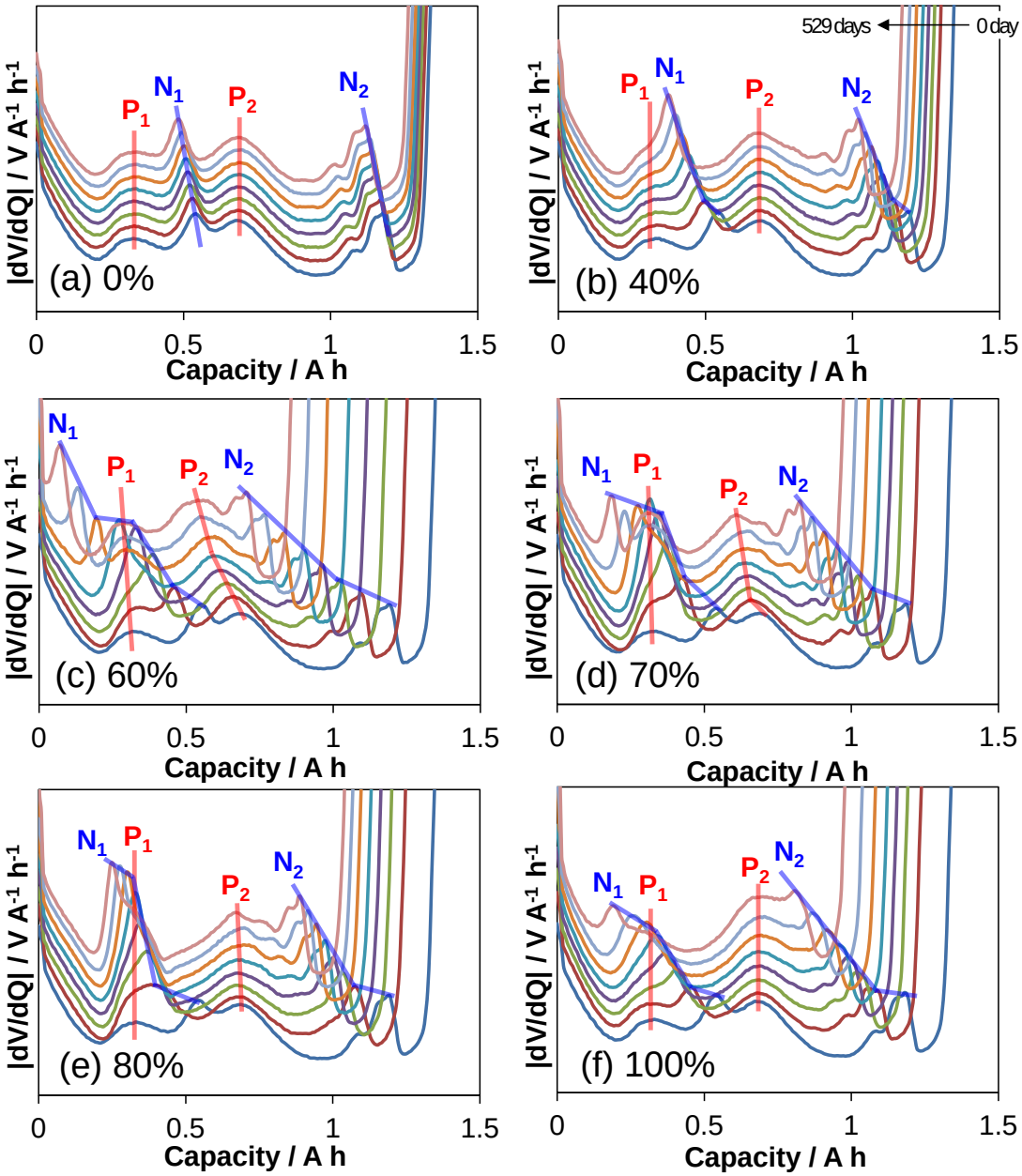

Figure 7. Changes of dV/dQ curve shapes during the storage life tests at 45°C.

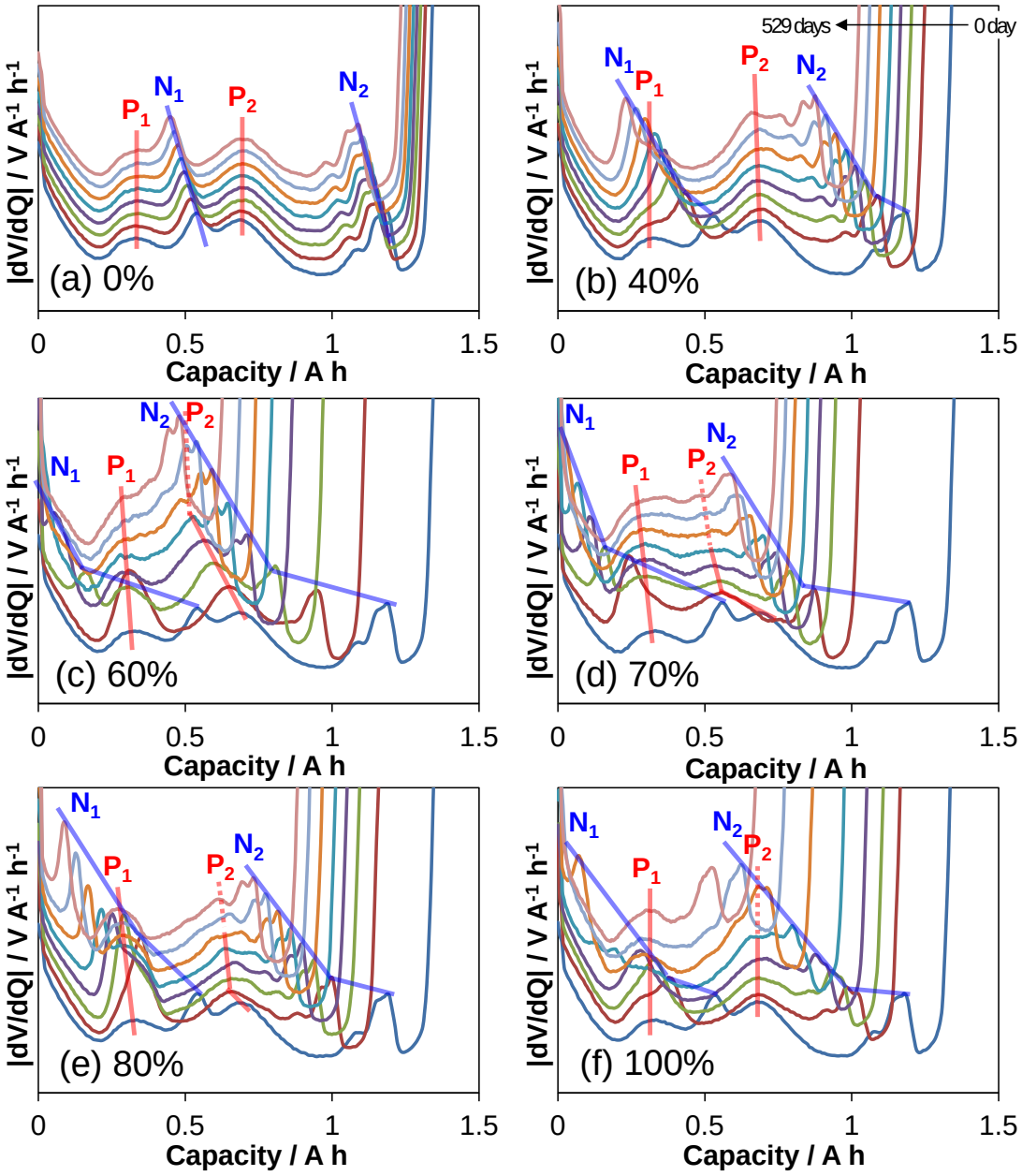

Figure 8. Changes of dV/dQ curve shapes during the storage life tests at 60°C.

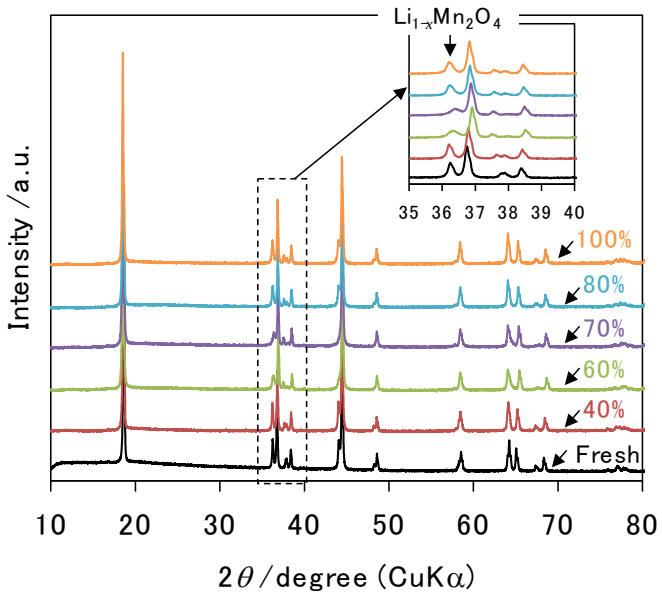

Figure 9. Powder x-ray diffraction patterns of positive electrode of fresh cell and after storage tests at 60°C for 176 days.

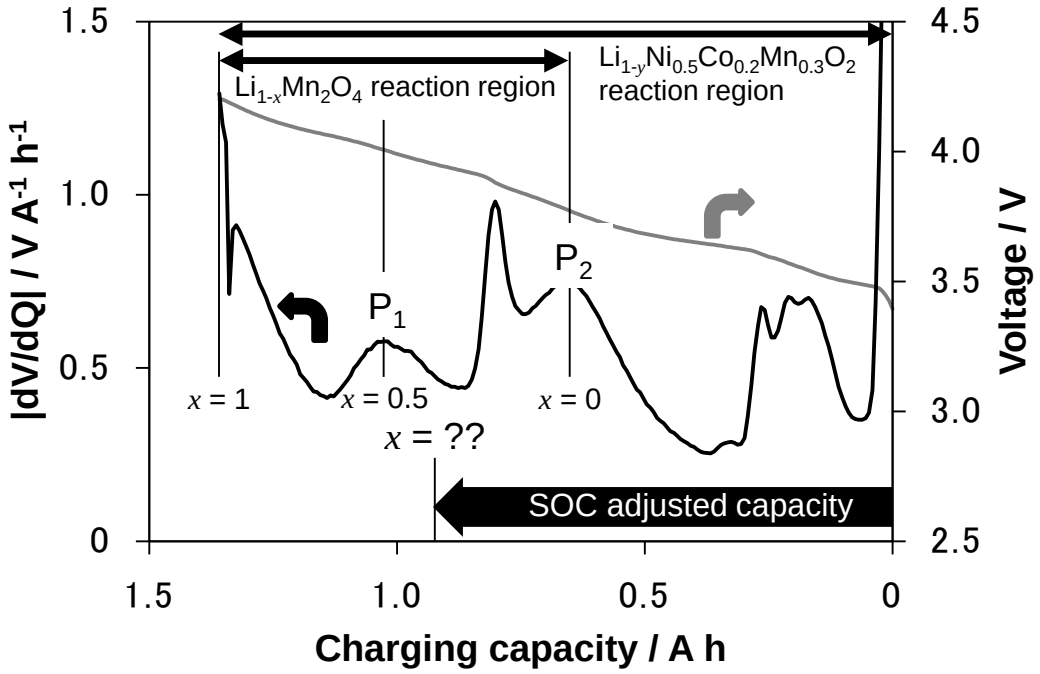

Figure 10. Estimate method of x value in $Li_{1-x}Mn_2O_4$.

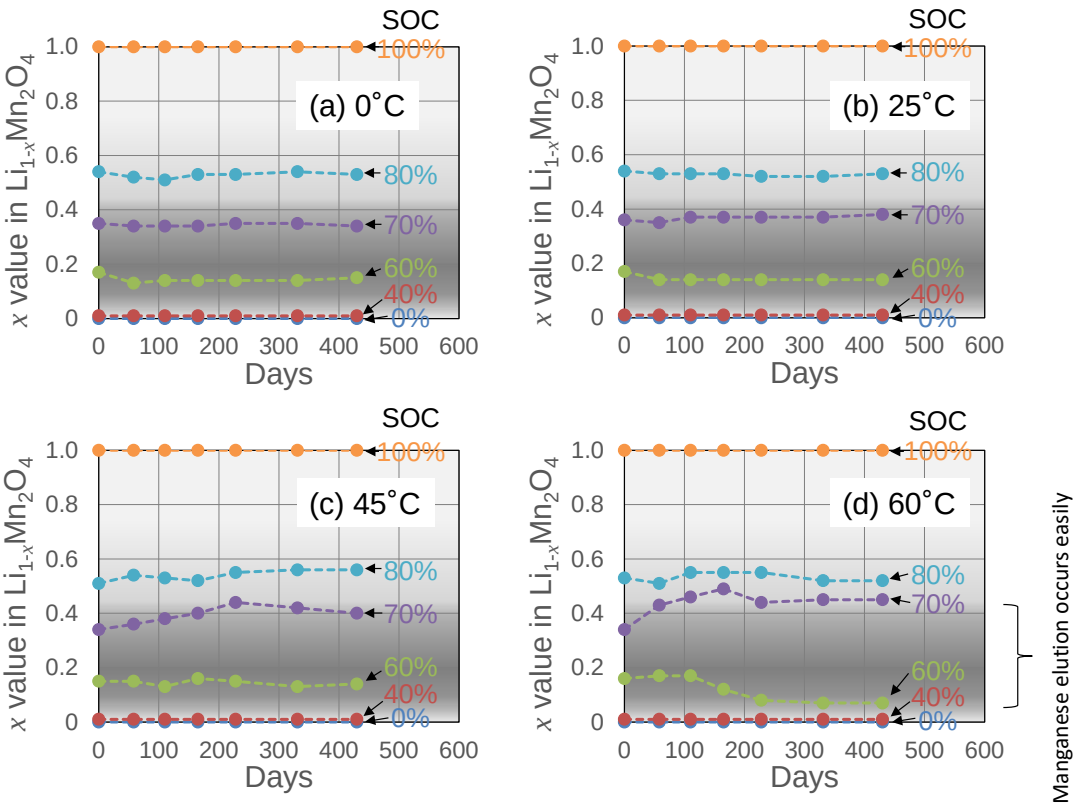

Figure 11. Changes of x value in $Li_{1-x}Mn_2O_4$ during the storage life tests at (a) 0°C, (b) 25°C, (c) 45°C, and (d) 60°C.

Chapter 3.

Degradation Diagnosis of Lithium-Ion Batteries with a $LiNi_{0.5}Co_{0.2}Mn_{0.3}O_2$ and $LiMn_2O_4$ Blended Positive Electrode Using dV/dQ Curve Analysis

3-1. Introduction

The widespread use of electric drive vehicles (xEVs) with low environmental impacts is crucial for the development of sustainable societies. Among the various types of xEVs, the use of battery electric vehicles (BEVs) with lithium-ion batteries is expected to significantly increase in the upcoming years. However, the limited cruising range (capacity of batteries), battery safety, and performance degradation (battery life) hamper the normalization of BEVs. Since BEVs are subjected to various environments which cause batteries degradation, such as acceleration and deceleration, quick charge, and wide temperature range (from −40°C to 80°C), an improvement in batteries durability is needed.

A thorough understanding of the degradation factors of lithium-ion batteries would allow enhancing their durability. These factors are divided into three main categories: (1) positive electrode degradation, (2) negative electrode degradation, and

(3) solid electrolyte interface (SEI) formation. Causes of positive electrode and negative electrode degradation include deactivation of active materials due to changes in the surface structure of particles [1,2] and the electronic disconnection between the active materials and a conductive carbon network or a current collector [3–7]. SEI formation probably occurs because side reactions such as decomposition of electrolyte solution [8] or lithium-metal deposition [9,10] result in an irreversible lithium-ion form. To date, there are few reports concerning the understanding of the influence of these degrading factors from a quantitative perspective, even though this is a fundamental issue. An example of quantitative analytical methods to assess the negative electrode and positive electrode degradation is the dV/dQ curve analysis, which is obtained from the differentiation of the charge/discharge curve (voltage–capacity curve). The analysis of battery degradation using dV/dQ curves has been reported for $LiNi_{1-x-y}Co_xAl_yO_2$/graphite [11], $LiNi_{1-x-y}Co_xMn_yO_2$/hard carbon [12], and $LiCoO_2$/graphite batteries [13]. On the other hand, the half-cell technique of the positive electrode and negative electrode of the disassembled battery can also be used for degradation analysis [14]. Contrary to the battery disassembling method, the dV/dQ curve analysis is nondestructive. Moreover, the dV/dQ curve analysis has the average information of the degradation over a whole battery, while the half-cell estimates have

the local information due to the electrode sampling.

Lithium-ion batteries for BEVs and plug-in hybrid electric vehicles often use a blended positive electrode (layered-materials and spinel-material) [15,16]. However, investigation on the degradation using dV/dQ curves is scarce for lithium-ion batteries with blended positive electrodes because conventional dV/dQ analysis is difficult to separate the positive electrode materials simultaneously reacting in the blend. In a previous report, I studied the specific storage degradation at middle state-of-charge (SOC) and the causes of the degradation rate changes via dV/dQ analysis of lithium-ion batteries with a blended positive electrode and a graphite negative electrode [17]. In this study, I developed a dV/dQ curve analysis for lithium-ion batteries with blended positive electrodes employing a separation technique for the materials of the positive electrode. Using the dV/dQ analysis, I were able to quantitatively and nondestructively analyze the positive electrode and negative electrode degradation and the SEI formation. Furthermore, by comparing the degradation of lithium-ion batteries under different cycle test conditions, the relation between the conditions and degradation factors was elucidated.

3-2. Experimental

3-2-1. Battery

A commercially available lithium-ion cell with a blended positive electrode (18650-type, 1.4 Ah) was used for the cycle tests. The cell was opened, and the electrode and electrolyte solution were analyzed. The cross section of the positive electrode, manipulated with an ion-milling system E-3500 (Hitachi High-Technologies), was observed using a field emission scanning electron microscope (FE-SEM, S8020 model, Hitachi High-Technologies) with energy-dispersive X-ray spectroscopy (EDX, X-Max 80 model Horiba). The mixed state maps and compositions of the two active materials in the positive electrode were analyzed by EDX. The crystal structures of the positive electrode and negative electrode were analyzed using an X-ray diffractometer (XRD, SmartLab, Rigaku) with Cu-Kα radiation at 40 kV and 30 mA. The XRD pattern was recorded at a scan rate of 5°/min in the 2θ range of 10°–120°. The ratio of the compounds in the positive electrode was quantitatively estimated by Rietveld analysis using the RIETAN-FP software [18]. The electrolyte solution, which was collected from centrifugation, was analyzed by gas chromatography-mass spectrometry (GC/MS, HP6890 and HP5973, Agilent Technologies) and nuclear magnetic resonance (NMR, JNM-LA400 model, JEOL).

Electrochemical properties were investigated using coin cells. A fresh cell was

opened, and the positive electrode and negative electrode were removed from the inside and washed with dimethyl carbonate. Then, a coin cell was assembled using the removed negative electrode or positive electrode as the working electrode, lithium foil as the counter electrode and 1 mol dm^{-3} lithium hexafluorophosphate ($LiPF_6$) in diethyl carbonate (DEC) and ethylene carbonate (EC) (1:1 in vol.) as an electrolytic solution. The charge/ discharge tests of the positive electrode and negative electrode half-cells were respectively performed in a potential range of 4.4–3.25 V vs. Li/Li^+ and 0.001–0.15 V vs. Li/Li^+ at a C/20 rate.

3-2-2. Cycle tests

The conditions of the cycle tests are shown in Table 1. They include one charge/discharge rate (C/3), two SOC ranges (100%–0% and 100%–70%), and three temperatures (0°C, 25°C, and 45°C). I used a total of 18 cells which 3 cells for each cycle condition in the cycle tests to confirm the reproducibly. SOC 100% and 0% were respectively 4.2 V constant current and constant voltage (CC-CV) charge and 2.5 V CC discharge. Voltages of SOC 70% at various temperatures were determined by discharging for 54 min at C/3 after fully charged (SOC 100%) at each temperature. There were 30 min rest steps after each charge and discharge step. The low current

charge/discharge test at C/20 at 25°C were performed every 40 cycles for the 100%–0% SOC range, and every 80 cycles for the 100%–70% SOC range. The low current charge/discharge test was evaluated every half month. The number of cycles was changed for the SOC ranges because the time for one cycle was different.

3-2-3. dV/dQ curve analysis for the blended positive electrode system

The dV/dQ curve analysis flow chart that was developed for the blended positive electrode is shown in Figure 1 (a). The initial data input were the dq/dV of the active materials of positive electrode (lithium nickel cobalt manganese oxide (NCM) and lithium manganese oxide (LMO)) and the active material of negative electrode (graphite). Each dq/dV was prepared from the half-cell charge/discharge test results of Section 2.1. The dq/dV of the blended positive electrode was separated according to the previous report [19], and the dq/dVs of NCM and LMO were obtained.

For the positive electrode, a $(dQ/dV)_P$ was obtained from Equation (1), which represents the addition of $(dq/dV)_{NCM}$ and $(dq/dV)_{LMO}$ each multiplied by the corresponding fitting parameters m_{NCM} and m_{LMO}. The $(dV/dQ)_P$ was the inverse of the $(dQ/dV)_P$. For the negative electrode, the $(dQ/dV)_N$ was similarly obtained: multiplying the $(dq/dV)_{Gr.}$ by the fitting parameter $m_{Gr.}$ (Equation (2)). Then, after inversing the

$(dQ/dV)_N$, the $(dV/dQ)_N$ was obtained.

$$\left(\frac{dQ}{dV}\right)_P \ [A\ h\ V^{-1}] = m_{NCM}\ [g] \times \left(\frac{dq}{dV}\right)_{NCM}\ [A\ h\ g^{-1}\ V^{-1}] + m_{LMO}\ [g] \times \left(\frac{dq}{dV}\right)_{LMO}\ [A\ h\ g^{-1}\ V^{-1}] \quad (1)$$

$$\left(\frac{dQ}{dV}\right)_N \ [A\ h\ V^{-1}] = m_{Gr.}\ [g] \times \left(\frac{dq}{dV}\right)_{Gr.}\ [A\ h\ g^{-1}\ V^{-1}] \quad (2)$$

Here, q_{NCM}, q_{LMO}, and $q_{Gr.}$ are the unit discharge capacity ([A h g^{-1}]) of each active material, and m_{NCM}, m_{LMO}, and $m_{Gr.}$ are the usable active material masses ([g]).

δ_P ([A h]) and δ_N ([A h]) are the fitting parameters to adjust the reaction region as shown in Figure 1 (b). $(dV/dQ)_{Cell\ sim.}$ is then obtained from the difference between $(dV/dQ)_P$ and $(dV/dQ)_N$ according to Equation (3):

$$\left(\frac{dV}{dQ}\right)_{Cell\ sim.} [V\ A^{-1}\ h^{-1}\ ] = \left(\frac{dV}{dQ}\right)_P [V\ A^{-1}\ h^{-1}\ ] - \left(\frac{dV}{dQ}\right)_N\ [V\ A^{-1}\ h^{-1}\ ] \quad (3)$$

By comparing the simulated results, $(dV/dQ)_{Cell\ sim.}$ with the experimental results, $(dV/dQ)_{Cell\ exp.}$ obtained from the low current charge/discharge tests, the five parameters (m_{NCM}, m_{LMO}, $m_{Gr.}$, δ_N, and δ_P) were optimized. For this, the initial values of m_{NCM} and m_{LMO} were estimated by fitting from the peak width and shape of the $(dV/dQ)_P$, and for $m_{Gr.}$, the initial value was also estimated by fitting from the peak width and shape of the $(dV/dQ)_N$. Then, the initial values of δ_P and δ_N were estimated from the respective peak positions. Afterward, the five parameters were fitted to the least squares method so as to minimize the error from the experimental data.

3-3. Results and discussion

3-3-1. Chemical analysis of the battery

The SEM image and EDX mapping of the positive electrode cross section are shown in Figure 2. Two kinds of particles with different shapes are observed. The EDX analysis results show that one particle comprises nickel, cobalt, and manganese as the transition metals, with a ratio of 5:2:3 (Ni:Co:Mn), whereas the other particle has only manganese as the transition metal. The XRD of the positive electrode and the Rietveld analysis to examine the ratio of the two active materials are shown in Figure 3. The XRD shows two patterns, which correspond to the *R*3*m* and *Fd*3*m* space groups, and the resulting Rietveld analysis suggests that the content is approximately 78:22 wt%. Both the XRD and SEM-EDX results indicate that the active materials of the positive electrode are $LiNi_{0.5}Co_{0.2}Mn_{0.3}O_2$ (NCM) and $LiMn_2O_4$ (LMO) in approximately 78:22 wt%. The XRD of the negative electrode implies that it contains graphite as the active material. The GC/MS and ^{1}H-/^{19}F NMR spectra of the electrolyte solution suggest that it consisted of dimethyl carbonate (DMC), ethyl methyl carbonate, and EC as solvents, fluoroethylene carbonate (FEC) as the additive, and approximately 1 mol dm^{-3} $LiPF_6$ as the electrolyte.

Figure 4 shows the dq/dV curves of the positive electrode and negative electrode

obtained from the discharge curves of the half-cells and the dq/dV curves of NCM and LMO obtained by separating the dq/dV curve of positive electrode (Figure 4 (c)). Three peaks are observed in the dq/dV curve of the positive electrode: the peak around 3.75 V vs. Li/Li^+ corresponds to the reaction of NCM [20], and the two peaks at approximately 4.0 and 4.15 V vs. Li/Li^+ correspond to the step reactions of LMO during phase change [21]. Three peaks are also observed in the dq/dV curve of the negative electrode, which show the stage structure changes of graphite (0.10 V: stage I→stage II, 0.14 V: stage II→stage III & IV, and 0.23 V: stage III & IV→Graphite) [22]. Using these dq/dV data, the dV/dQ curve analysis was performed as indicated in Section 2.3.

3-3-2. Cycle tests

The capacity retention of the representative cell in 3 cells for each cycle condition during cycle tests is shown in Figure 5, as it is confirmed that the capacity retentions of 3 cells for each cycle condition are almost same. To compare the 6 test conditions which were differences the discharge capacity per cycle, the equivalent cycle number is indicated in the x axis; it was calculated by the integration of the discharge capacity divided by the typical capacity (1.402 A h). When looking at the 200 equivalent cycles point, the capacity retention at 45°C is 87% and 91% for the SOC ranges of

100%–70% and 100%–0%, respectively. Then, at 25°C, it was 93% and 94%, respectively, for 100%–70% and 100%–0%. Finally, at 0°C, it was 94% for both SOC ranges. At high temperatures, the decrease in the capacity retention was faster than at low temperatures. Considering the same temperature, the capacity for the 100%–70% SOC range decreased faster than that for the 100%–0% SOC range. However, this difference was less pronounced as the temperature decreased. The degradation rates at 0°C were very similar, regardless of the SOC range.

3-3-3. dV/dQ curve analysis

The dV/dQ curve analyses were conducted to quantitatively evaluate the influence of temperature and SOC range on the cycle test results. The dV/dQ curve analysis of the initial cell is shown in Figure 6. The simulated curve adequately fitted the experimental results, thus confirming that the fitting method was suitable for the process. As seen in the initial dV/dQ curve analysis, there are two peaks for both the positive electrode and negative electrode. For the positive electrode, one of the peaks (P_1) shows a phase change of $LiMn_2O_4$ while the other peak (P_2) indicates a change in main reactive species from LMO to NCM [12]. The peaks N_1 and N_2 for the negative electrode correspond to the graphite stage structures [22]. The dV/dQ curve analysis

from the finished cycle tests under various conditions are shown in Figure 7. As can be seen in the figure, the peak intensity is deviated from the experimental data, particularly N_1, which becomes sharp. However, the remaining peaks and their positions are well fitted. Changes of each five fitting parameters are shown in Figure 8. It is confirmed by Figure 7 and Figure 8 that δ_N increase at all conditions, and masses of NCM decrease at the 100%–0% SOC range.

Capacity retention of the negative electrode and positive electrode which were calculated using evolution $m_{Gr.} \times q_{Gr.}$ and $m_{NCM} \times q_{NCM} + m_{LMO} \times q_{LMO}$, respectively, are shown in Figure 9. The negative electrode capacities decreased about 2% in the early cycles and kept slowly decreasing afterward under all conditions. Capacity maintenance rates of the negative electrode did not generally depend on any condition tested. The positive electrode capacities decreased for the 100%–0% SOC range; however, they hardly decreased for the 100%–70% SOC range. Capacity retention rates of the positive electrode depended only on the SOC range but not on the temperature. The results of the separation of the positive electrode capacity into NCM and LMO are shown in Figure 10. The drop in the positive electrode capacity at the 100%–0% SOC range was caused by the degradation of the NCM.

To compare the dV/dQ curve analysis results with the half-cell technique [14],

the cells that were evaluated in the cycle test at the 100%–0% SOC range were disassembled and the capacity of the removed positive electrode were measured using the half-cells. They degraded to about 90%–93% compared with initial. This result supports the dV/dQ curve analysis results. The positive electrode cross section SEM images are shown in Figure 11. After the cycle test, particularly for the 100%–0% SOC range (Figure 11 (b)), several cracks were found inside the NCM particles. For the LMO particles, there was no significant difference before and after the cycle tests. This is considered to be due to the spinel compounds such as LMO has stable host structure at room temperature [23], and due to the staying time at specific SOC that LMO can be degraded easily [17] has been short in the cycle test. Further, I discuss the differences in the degree of contribution of degradation factors. The degradation factors were quantitatively divided into (1) positive electrode degradation, (2) negative electrode degradation, and (3) SEI formation. I considered that the capacity of lithium-ion batteries is nearly the same as the amount of active Li^+ ions in the system (Fig. 8 (upper)). Consequently, the capacity decrease of the battery ($\Delta capacity_{Cell}$) is expressed as follows using the loss of active Li^+ ions (ΔLi_{Cell}) (Equation (4)).

$$\Delta capacity_{Cell}\ [Ah] = \frac{F\ [s\ A\ mol^{-1}] \times \Delta Li_{Cell}[g]}{3600\ [s\ h^{-1}] \times M_{Li}[g\ mol^{-1}]} \quad (4)$$

Where F is the Faraday constant and M_{Li} is the atomic mass of lithium. The loss of

active Li^+ ions is expressed as summation of the deactivated positive electrode material (ΔLi_P) and deactivated negative electrode material (ΔLi_N) and by the SEI formed from side reactions (ΔLi_{SEI}) (Equation (5)).

$$\Delta Li_{Cell}[g] = \Delta Li_P[g] + \Delta Li_N[g] + \Delta Li_{SEI}[g] \qquad (5)$$

I consider that ΔLi_P and the capacity decrease of the positive electrode are correlated and that ΔLi_N and the capacity decrease of the negative electrode are correlated. Accordingly, I propose that ΔLi_P (or ΔLi_N) is calculated from the decreased capacity of the positive electrode (or negative electrode) multiplied by the average Li^+ ion percentage in the positive electrode (negative electrode) active materials during cycle tests as follows Equations (6) and (7).

$$\Delta Li_P[g] = \frac{3600\ [s\ h^{-1}] \times M_{Li}[g\ mol^{-1}]}{F\ [s\ A\ mol^{-1}]}\left((\text{Li content rate})_{NCM} \times \Delta\text{Capacity}_{NCM}[Ah] + (\text{Li content rate})_{LMO} \times \Delta\text{Capacity}_{LMO}[Ah]\right) \qquad (6)$$

$$\Delta Li_N[g] = \frac{3600\ [s\ h^{-1}] \times M_{Li}[g\ mol^{-1}]}{F\ [s\ A\ mol^{-1}]}\left((\text{Li content rate})_{Gr.} \times \Delta\text{Capacity}_{Gr.}[Ah]\right) \qquad (7)$$

The average Li^+ ion content was calculated at the mid values of each SOC range (corresponding to a 50% and 85% for the 100%–0% and 100%–70% SOC ranges, respectively) in the positive electrode (or the negative electrode) utilization region, which was obtained from the dV/dQ curve analysis.

The ΔLi_{SEI} is calculated from Equation (5) using ΔLi_{Cell}, ΔLi_P and ΔLi_N obtained from Equations (4), (6) and (7). The results obtained when changing the ratios

of the active Li^+ ion loss in the deactivated positive electrode and negative electrode and the formed SEI are shown in Figure 12 (lower).

A comparison within the 100%–0% SOC range (0°C, 25°C, and 45°C) indicates that equal degradation of the positive electrode and negative electrode occurred, regardless of the temperature; however, the degree of SEI increased when temperature increased. For the 100%–70% SOC range, the battery capacity decreases almost because of SEI formation. At higher temperatures, the capacity decrease was faster than at lower temperatures. Comparing the results at the same temperature, the amount of SEI was larger for the 100%–70% than for the 100%–0% SOC range. As seen in Figure 5, the rate of capacity decrease at 0°C was the same for both SOC ranges. However, according to the results mentioned above, the degradation mechanisms were not same. For the 100%–0% SOC range, both positive electrode capacity decrease and SEI formation due to side reactions mainly occurred and negative electrode capacity also decreased. Meanwhile, for the 100%–70% SOC range, positive electrode capacity decrease was hardly observed and the SEI formation and negative electrode capacity decrease were occurred.

3-3-4. Analysis of usage conditions and the degradation mechanisms

Unlike previous storage tests in which the degradation of the positive electrode depended on both the SOC and temperature [17], in the present study, the degradation of the positive electrode depends on the SOC range, regardless of temperature. For the 100%–0% SOC range, the degradation is due to NCM, and I concluded that the electronic isolation and/or deactivation occurred because of the micro cracks inside the NCM, as seen via SEM; cracks may be the result of repeated expansion and contraction [14]. The expansion and contraction coefficient in one cycle is larger in the 100%–0% than in the 100%–70% SOC range [24]; therefore, the positive electrode capacity decrease in the former is accelerated. This coefficient hardly depends on temperature.

The degradation of the negative electrode does not depend on the cycle conditions, and its influence is relatively small compared to the other two degradation factors. Honkura et al. confirmed that changes in the peak shapes of the graphite dV/dQ curve occurred due to repeated charge and discharge [13] and not due to degradation. The degradation mechanismof the graphite negative electrode has been reported as the destruction of the layer structure due to the penetration of solvent molecules between graphite layers or the isolation from the reaction system after SEI growth or the breakdown of the electrode structure due to expansion and contraction of graphite by charging and discharging [25,26]. I consider that the degradation of the negative

electrode arose from these phenomena.

SEI formation is faster when the test temperature is higher. This is believed to be due to the decomposition of the electrolyte solution, which results in SEI formation, as it is known that the reductive decomposition reaction is accelerated at high temperature [17]. Furthermore, this SEI formation is more noticeable in the 100%–70% SOC range. This may be due to the longer retention time at higher SOC, which proceeds with the reduction decomposition reaction on the negative electrode surface [17].

3-4. Conclusion

In this study, a dV/dQ curve analysis was developed for a blended positive electrode. By adapting the analysis for lithium-ion batteries with blended positive electrodes, I quantitatively evaluated the degradation factors under different cycle test conditions. I confirmed that there are clear differences in the degree of contribution of the different degradation factors depending on the conditions. For instance, at 0°C, although the capacity reduction rate was almost same regardless of the SOC range, the degradation mechanisms were different. For the 100%–0% SOC range, the positive electrode and negative electrode degradation and the SEI formation occurred at the same time, resulting in the reduced capacity. Meanwhile, for the 100%–70% SOC range, capacity

reduction was mainly due to SEI formation. The nondestructive quantitative evaluation of the degradation factors of batteries is useful to determine the relation between usage conditions and degradation factors. I expect to achieve accurate accelerated tests and lifetime prediction methods based on this study.

References

[1] Y. Makimura, S. Zheng, Y. Ikuhara, Y. Ukyo, Microstructural observation of $LiNi_{0.8}Co_{0.15}Al_{0.05}O_2$ after charge and discharge by scanning transmission electron microscopy, J. Electrochem. Soc. 159 (2012) A1070–A1073. DOI: 10.1149/2.073207jes

[2] S. Watanabe, M. Kinoshita, T. Hosokawa, K. Morigaki, K. Nakura, Capacity fading of $LiAl_yNi_{1-x-y}Co_xO_2$ cathode for lithium-ion batteries during accelerated calendar and cycle life tests (effect of depth of discharge in charge–discharge cycling on the suppression of the micro-crack generation of $LiAl_yNi_{1-x-y}Co_xO_2$ particle), J. Power Sources. 260 (2014) 50–56. DOI: 10.1016/j.jpowsour.2014.02.103

[3] C. Wang, A.J. Appleby, F.E. Little, Electrochemical study on nano-Sn, $Li_{4.4}Sn$ and $AlSi_{0.1}$ powders used as secondary lithium battery anodes, J. Power Sources. 93 (2001) 174–185. DOI: 10.1016/S0378-7753(00)00576-0

[4] J.H. Ryu, J.W. Kim, Y.-E. Sung, S.M. Oh, Failure Modes of Silicon Powder Negative Electrode in Lithium Secondary Batteries, Electrochemical and Solid-State Letters. 7 (2004) A306–A309. DOI: 10.1149/1.1792242

[5] J. Vetter, P. Novák, M.R. Wagner, C.Veit, K.-C. Möller, J.O. Besenhard, M. Winter, M.W.-Mehrens, C. Vogler, A. Hammouche, Ageing mechanisms in lithium-ion batteries, J. Power Sources. 147 (2005) 269–281. DOI: 10.1016/j.jpowsour.2005.01.006

[6] T. Waldmann, A. Iturrondobeitia, M. Kasper, N. Ghanbari, F. Aguesse, E. Bekaert, L. Daniel, S. Genies, I.J. Gordon, M.W. Loble, E.D. Vito, M.W.-Mehrens, Review—Post-Mortem Analysis of Aged Lithium-Ion Batteries: Disassembly Methodology and Physico-Chemical Analysis Techniques, J. Electrochem. Soc. 163 (2016) A2149–A2164. DOI: 10.1149/2.1211609jes,

[7] Y. Merla, B. Wu, V. Yufit, N.P. Brandon, R.F. Martinez-Botas, G.J. Offer, Novel application of differential thermal voltammetry as an in-depth state-of-health diagnosis method for lithium-ion batteries, J. Power Sources. 307 (2016) 308–319. DOI: 10.1016/j.jpowsour.2015.12.122

[8] V.A. Agubra, J.W. Fergus, The formation and stability of the solid electrolyte interface on the graphite anode, J. Power Sources. 268 (2014) 153–162. DOI: 10.1016/j.jpowsour.2014.06.024

[9] M.C. Smart, B.V. Ratnakumar, Effects of Electrolyte Composition on Lithium Plating in Lithium-Ion Cells, J. Electrochem. Soc. 158 (2011) A379–A389. DOI: 10.1149/1.3544439

[10] B.P. Matadi, , S. Geniès, A. Delaille, C. Chabrol, E.d. Vito, M. Bardet, J.-F. Martin, L. Daniel, Y. Bultel, Irreversible Capacity Loss of Li-Ion Batteries Cycled at Low

Temperature Due to an Untypical Layer Hindering Li Diffusion into Graphite Electrode, J. Electrochem. Soc. 164 (2017) A2374–A2389. DOI: 10.1149/2.0491712jes

[11] I. Bloom, A.N. Jansen, D.P. Abraham, K.L. Gering, Differential voltage analyses of high-power, lithium-ion cells 1. Technique and application, J. Power Sources. 139 (2005) 295–303. DOI: 10.1016/j.jpowsour.2004.07.021

[12] K. Honkura, K. Takahashi, T. Horiba, Capacity-fading prediction of lithium-ion batteries based on discharge curves analysis, J. Power Sources. 196 (2011) 10141–10147. DOI: 10.1016/j.jpowsour.2011.08.020

[13] K. Honkura, T. Horiba, Study of the deterioration mechanism of $LiCoO_2$/graphite cells in charge/discharge cycles using the discharge curve analysis, J. Power Sources. 264 (2014) 140–146. DOI: 10.1016/j.jpowsour.2014.04.036

[14] S. Watanabe, M. Kinoshita, T. Hosokawa, K. Morigaki, K. Nakura, Capacity fade of analysis of $LiAl_yNi_{1-x-y}Co_xO_2$ cathode for lithium-ion batteries during accelerated calendar and cycle life tests (surface analysis of $LiAl_yNi_{1-x-y}Co_xO_2$ cathode after cycle tests in restricted depth of discharge ranges), J. Power Sources. 258 (2014) 210–217. DOI: 10.1016/j.jpowsour.2014.02.018

[15] J. Belt, V. Utgikar, I. Bloom, Calendar and PHEV cycle life aging of high-energy, lithium-ion cells containing blended spinel and layered-oxide cathodes, J. Power Sources. 196 (2011) 10213–10221. DOI: 10.1016/j.jpowsour.2011.08.067

[16] A.C-Arenas, S. Onori, Y. Guezennec, G. Rizzoni, Capacity and power fade cycle-life model for plug-in hybrid electric vehicle lithium-ion battery cells containing blended spinel and layered-oxide positive electrodes, J. of Power Sources. 278 (2015) 473–483. DOI: 10.1016/j.jpowsour.2014.12.047

[17] K. Ando, T. Matsuda, M. Myojin, D. Imamura, Calendar Degradation Mechanism of Lithium Ion Batteries with a $LiMn_2O_4$ and $LiNi_{0.5}Co_{0.2}Mn_{0.3}O_2$ Blended Cathode, ECS Trans. 75 (2017) 77–90. DOI: 10.1149/07523.0077ecst

[18] F. Izumi, K. Momma, Three-dimensional visualization in powder diffraction, Solid State Phenom. 130 (2007) 15–20. DOI: 10.4028/www.scientific.net/SSP.130.15

[19] T. Kobayashi, N. Kawasaki, Y. Kobayashi, K. Shono, Y. Mita, H. Miyashiro, A method of separating the capacities of layer and spinel compounds in blended cathode, J. Power Sources. 245 (2014) 1–6. DOI: 10.1149/07523.0077ecst

[20] Y. Shi, M. Zhang, D. Qian, Y.S. Meng, Ultrathin Al_2O_3 coatings for improved cycling performance and thermal stability of $LiNi_{0.5}Co_{0.2}Mn_{0.3}O_2$ cathode material, Electrochem. Acta. 203 (2016) 154–161. DOI: 10.1016/j.electacta.2016.03.185

[21] T. Ohzuku, M. Kitagawa, T. Hirai, Electrochemistry of Manganese Dioxide in Lithium Nonaqueous Cell III. X‐Ray Diffractional Study on the Reduction of Spinel‐Related Manganese Dioxide, J. Electrochem. Soc. 137 (1990) 769–775. DOI: 10.1149/1.2086552

[22] J. R. Dahn, Phase diagram of Li_xC_6, Phys. Rev. B. 44 (1991) 9170. DOI: 10.1103/PhysRevB.44.9170

[23] M. M. Thackeray, Manganese oxides for lithium batteries, Prog. Solid State Chem. 25 (1997) 1-71.

[24] X.-L. Wang, K. An, L. Cai, Z. Feng, S.E. Nagler, C. Daniel, K.J. Rhodes, A.D. Stoica, H.D. Skorpenske, C. Liang, W. Zhang, J. Kim, Y. Qi, S.J. Harris, Visualizing the chemistry and structure dynamics in lithium-ion batteries by in-situ neutron diffraction, Sci. Rep. 2 (2012) 747. DOI: 10.1038/srep00747

[25] S.J. An, J. Li, C. Daniel, D. Mohanty, S. Nagpure, D.L. Wood, The state of understanding of the lithium-ion-battery graphite solid electrolyte interphase (SEI) and its relationship to formation cycling, Carbon. 105 (2016) 52–76. DOI: 10.1016/j.carbon.2016.04.008

[26] Y. Merla, B. Wu, V. Yufit, N.P. Brandon, R.F. Martinez-Botas, G.J. Offer, Novel application of differential thermal voltammetry as an in-depth state-of-health diagnosis

method for lithium-ion batteries, J. Power Sources. 307 (2016) 308–319. DOI: 10.1016/j.jpowsour.2015.12.122

Table 1. Cycle test conditions.

C rate	C/3
Charge / discharge	CCCV (C/20 or 30 min cut off)/CC
SoC range	100%–0%, 100%–70%
Temperature	0°C, 25°C, and 45°C

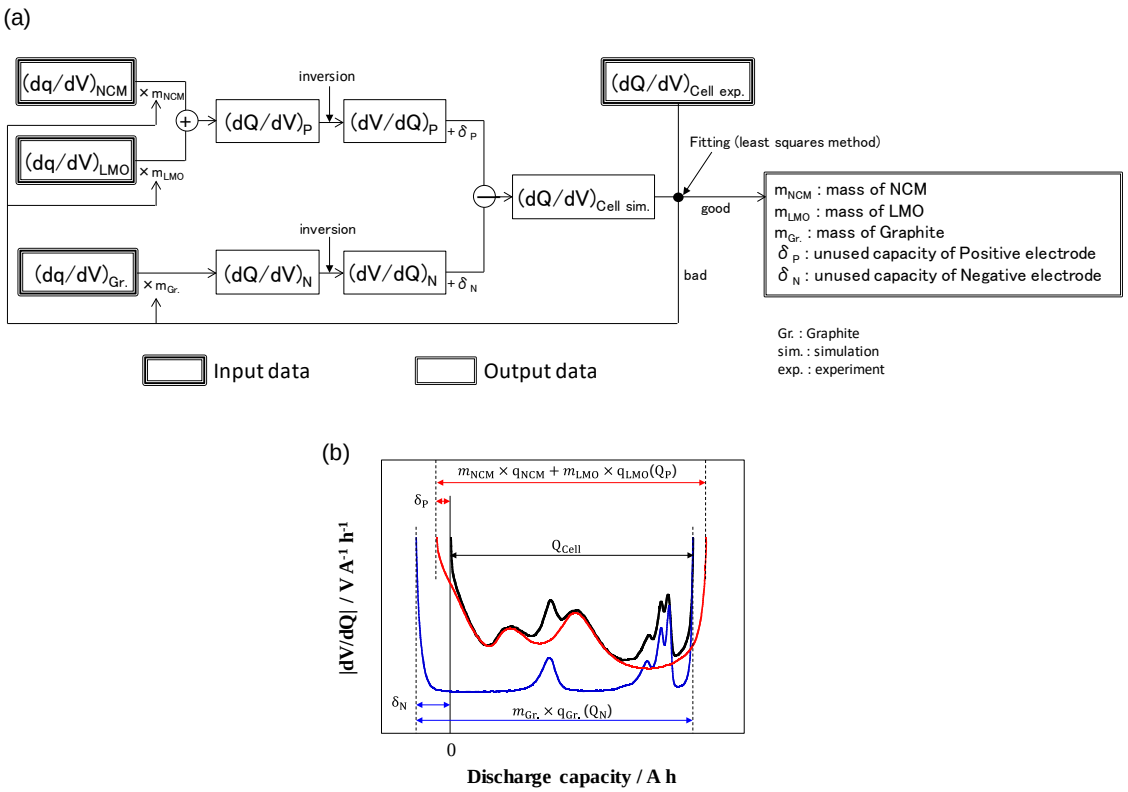

Figure 1. dV/dQ curve analysis flow chart adapted for the blended positive electrode (a) and an example of fitting results of the discharge curve (b).

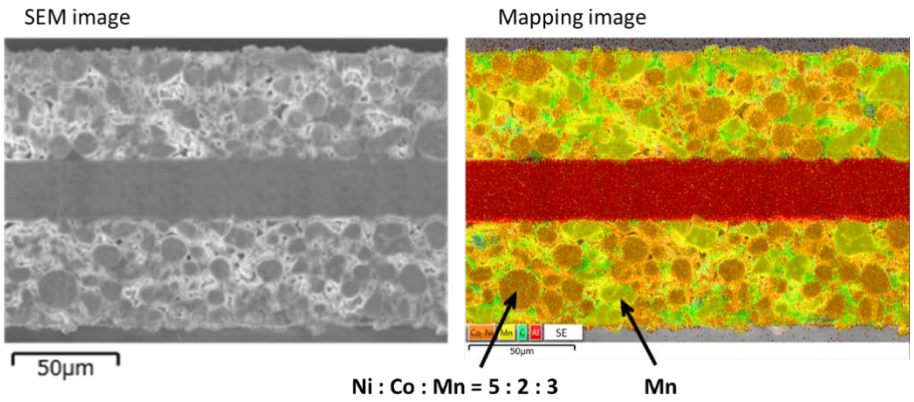

Figure 2. SEM image and the corresponding energy-dispersive X-ray spectroscopy (EDX) mapping of cobalt (orange), nickel (orange), manganese (yellow), carbon (green), and aluminum (red) in the cross section of the positive electrode.

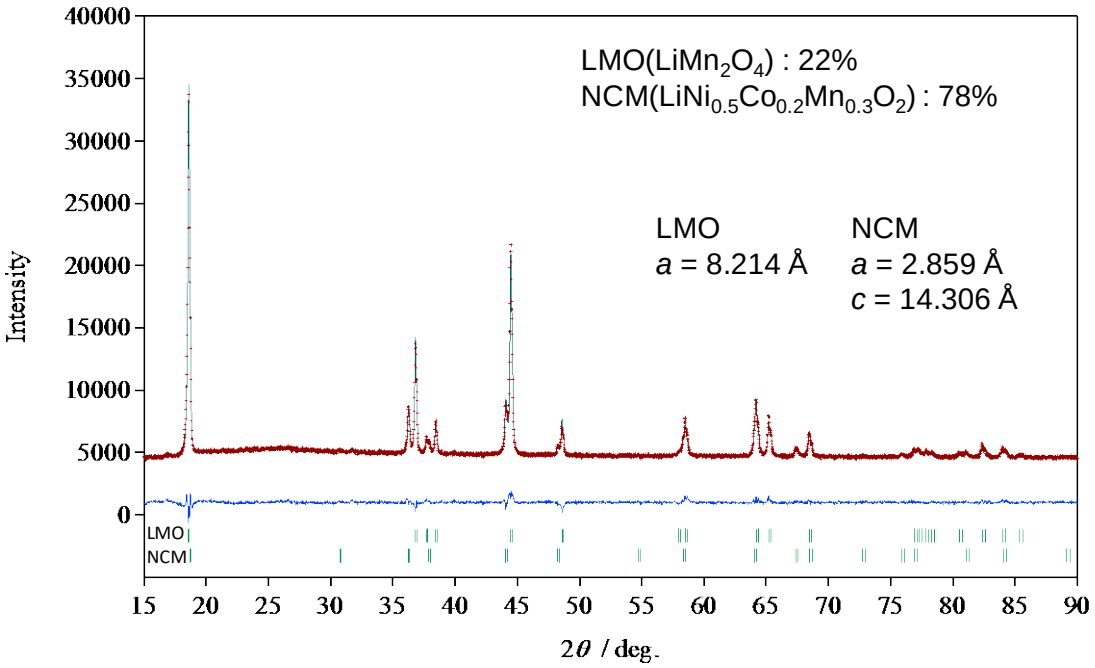

Figure 3. Rietveld refinement of blended positive electrode data; (red dots) experimental pattern, (black solid line) calculated pattern, (blue solid line) difference curve. Vertical bars represent the position of Bragg reflections at λ ≈ 1.5560 Å; (upper) $LiNi_{0.5}Co_{0.2}Mn_{0.3}O_2$ with space group *R*-3 m, (lower) $LiMn_2O4$ with space group *Fd*-3 m.

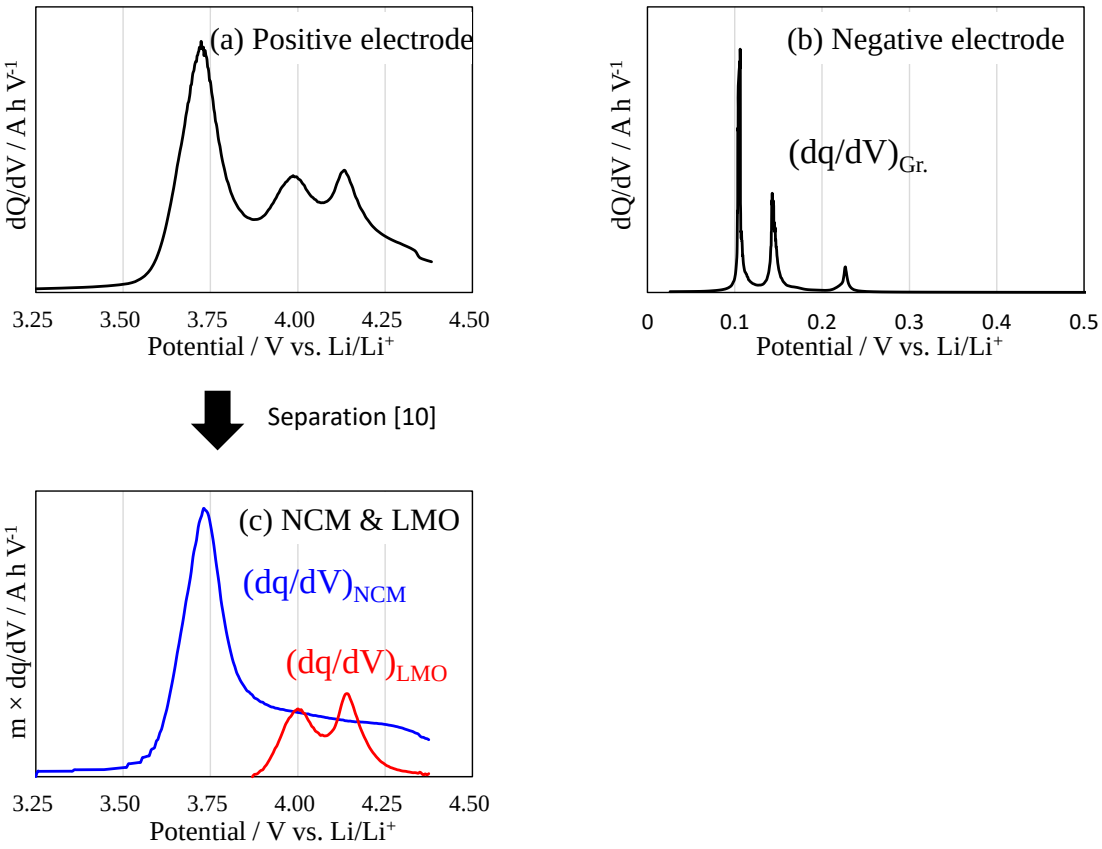

Figure 4. dq/dV curvess of (a) the positive electrode and (b) the negative electrode, and (c) dq/dV curves of the NCM and LMO obtained by separation of the positive electrode according to reference [10].

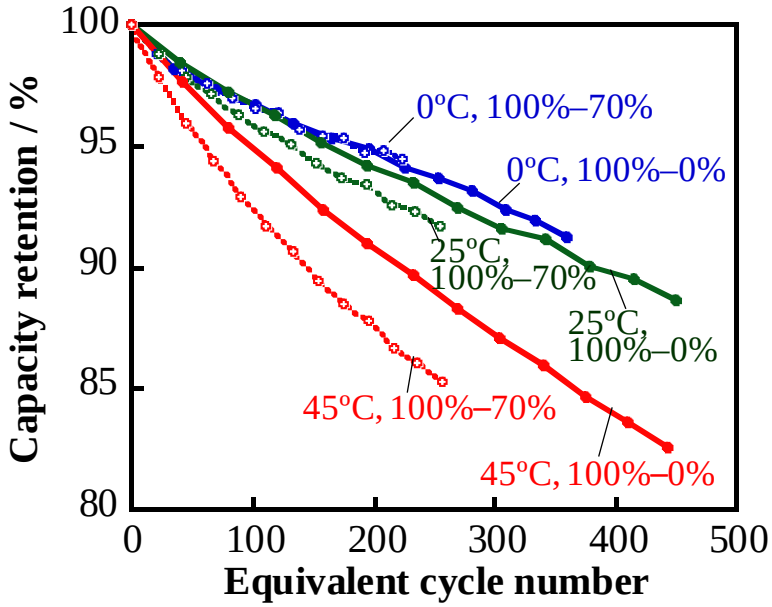

Figure 5. Capacity retention measured at various conditions.

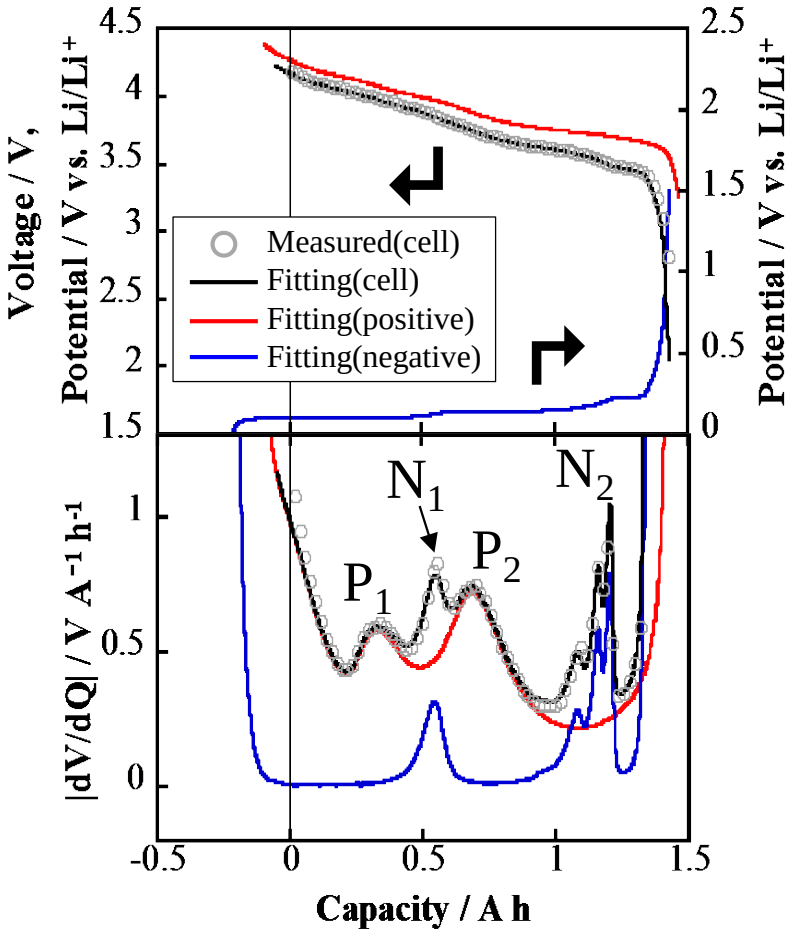

Figure 6. The results of the dV/dQ curve analysis of cells measured before tests.

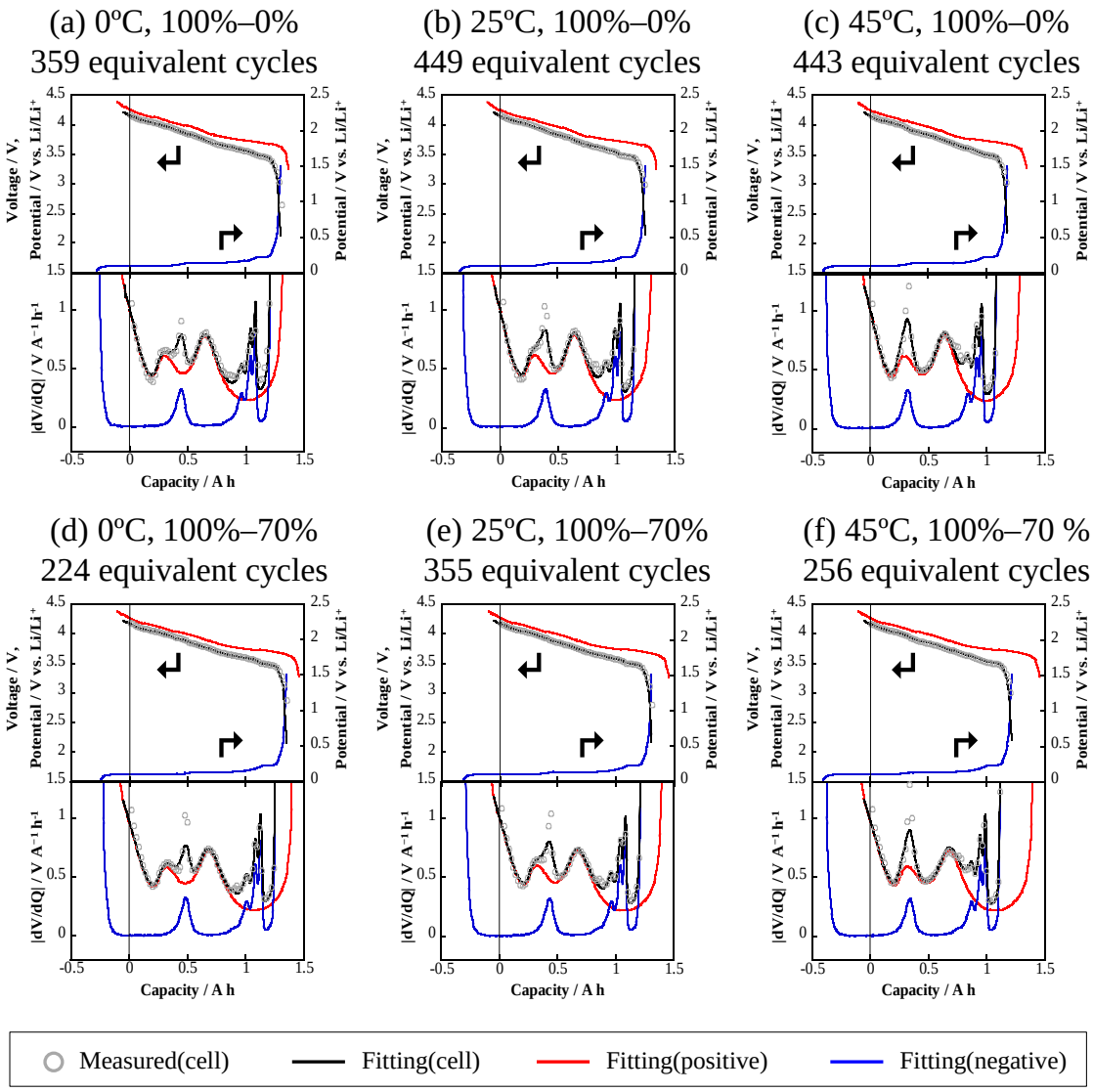

Figure 7. Results of the dV/dQ curve analysis of cells measured (a) after 359 equivalent cycles at 0 °C and 100%–0%, (b) after 449 equivalent cycles at 25 °C and 100%–0%, (c) after 443 equivalent cycles at 45 °C and 100%–0%, (d) after 224 equivalent cycles at 0 °C and 100%–0%, (e) after 355 equivalent cycles at 25 °C and 100%–70%, and (f) after 256 equivalent cycles at 45 °C and 100%–70%.

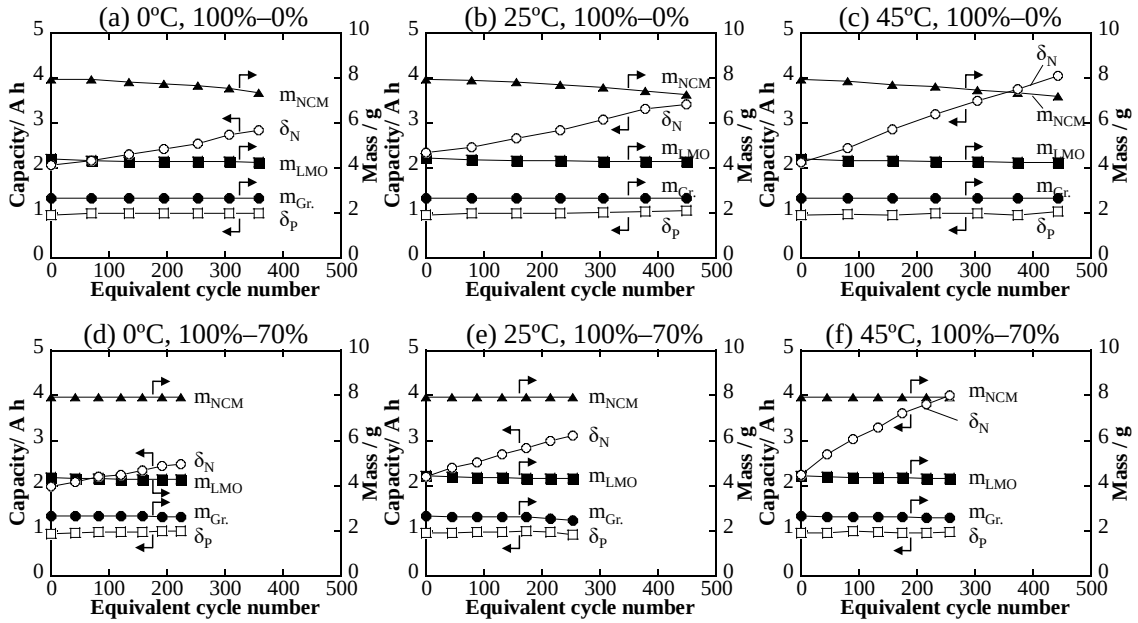

Figure 8. Change of five fitting parameters (m_{NCM}, m_{LMO}, $m_{Gr.}$, $\delta_{P,}$ and δ_N) in the cycling at (a) 0ºC and 100%–0%, (b) 25ºC and 100%–0%, (c) 45ºC and 100%–0%, (d) 0ºC and 100%–70%, (e) 25ºC and 100%–70%, and (f) 45ºC and 100%–70% estimated by dV/dQ curve analysis.

(a) Capacity retention of the negative electrode

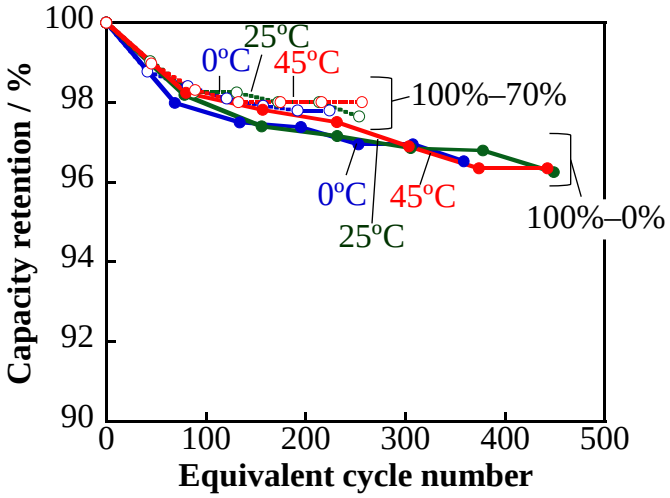

(b) Capacity retention of the positive electrode

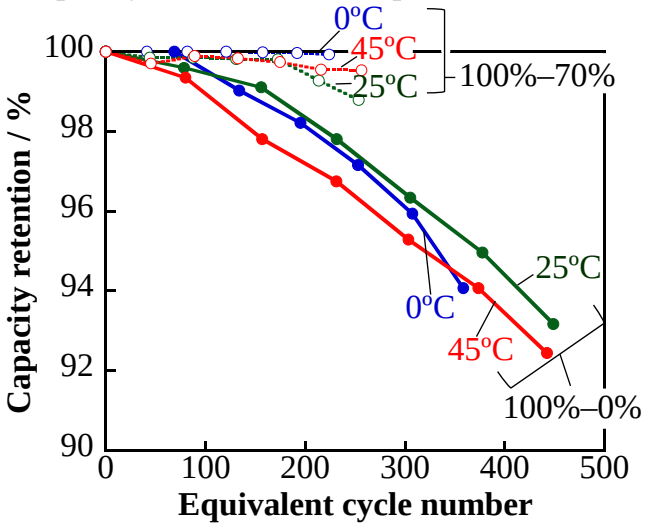

Figure 9. Capacity retention of the (a) positive electrode and (b) negative electrode at various conditions estimated from the dV/dQ curve analysis.

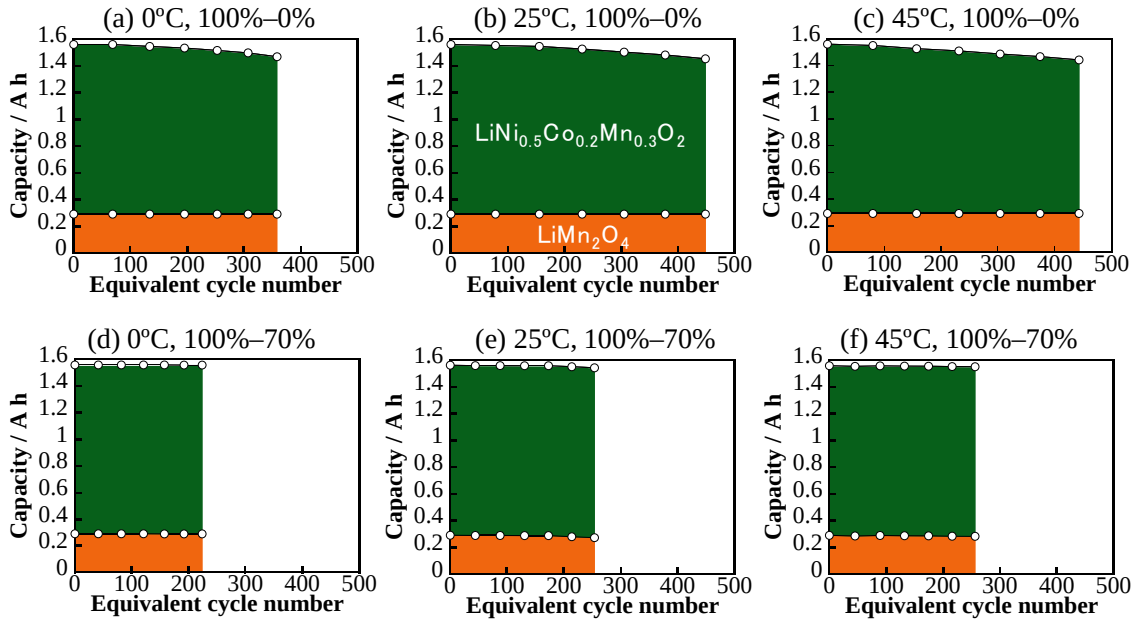

Figure 10. Capacity change of $LiNi_{0.5}Co_{0.2}Mn_{0.3}O_2$ and $LiMn_2O_4$ in the positive electrode at (a) 0 °C and 100%–0%, (b) 25 °C and 100%–0%, (c) 45 °C and 100%–0%, (d) 0 °C and 100%–70%, (e) 25 °C and 100%–70%, and (f) 45 °C and 100%–70% estimated from the dV/dQ curve analysis.

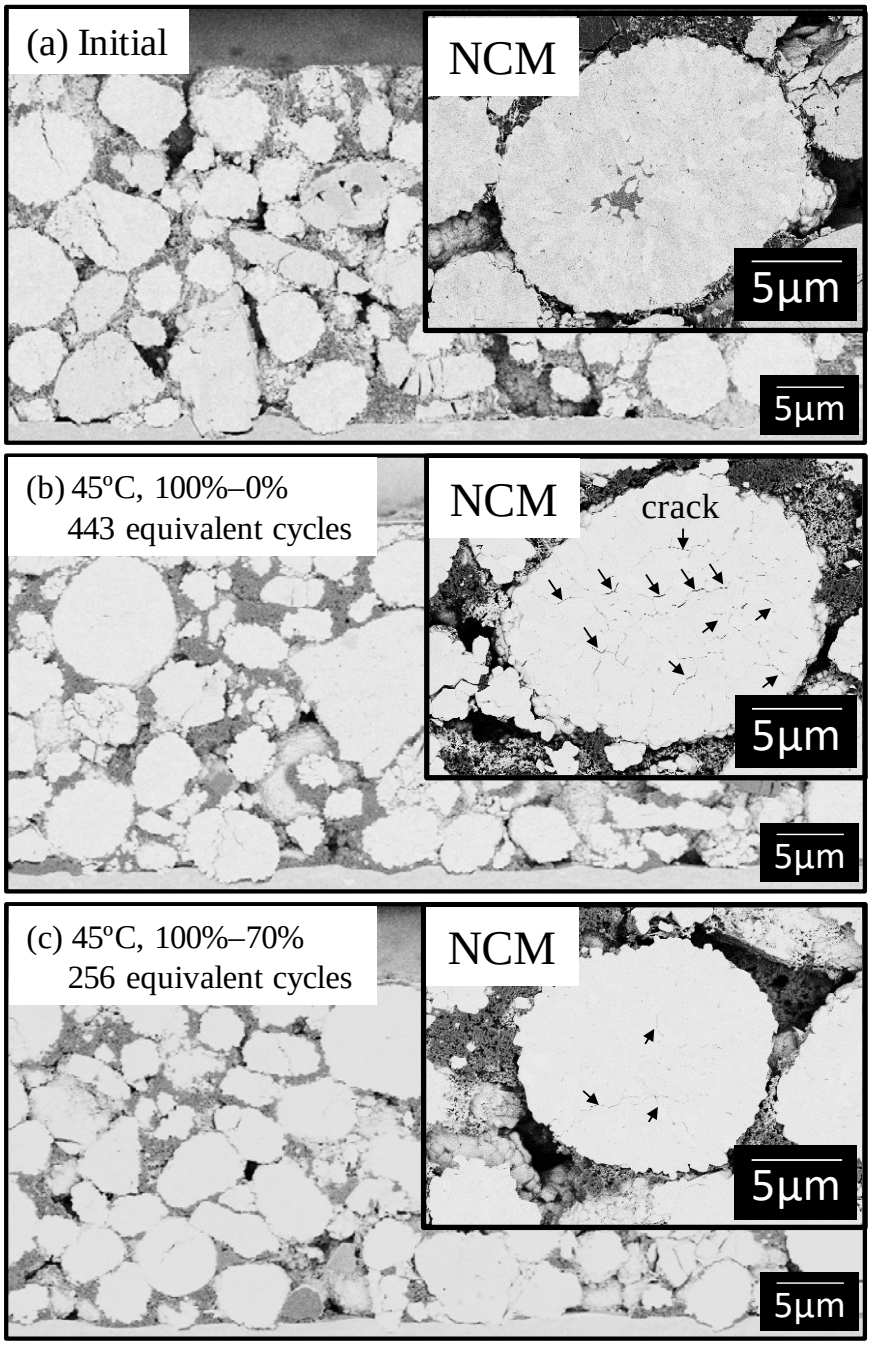

Figure 11. SEM images of the cross section of the positive electrode. (a) Initial cell and tested cells, (b) after 480 cycles at 45 °C and 100%–0%, and (c) after 960 cycles at 45 °C and 100%–70%.

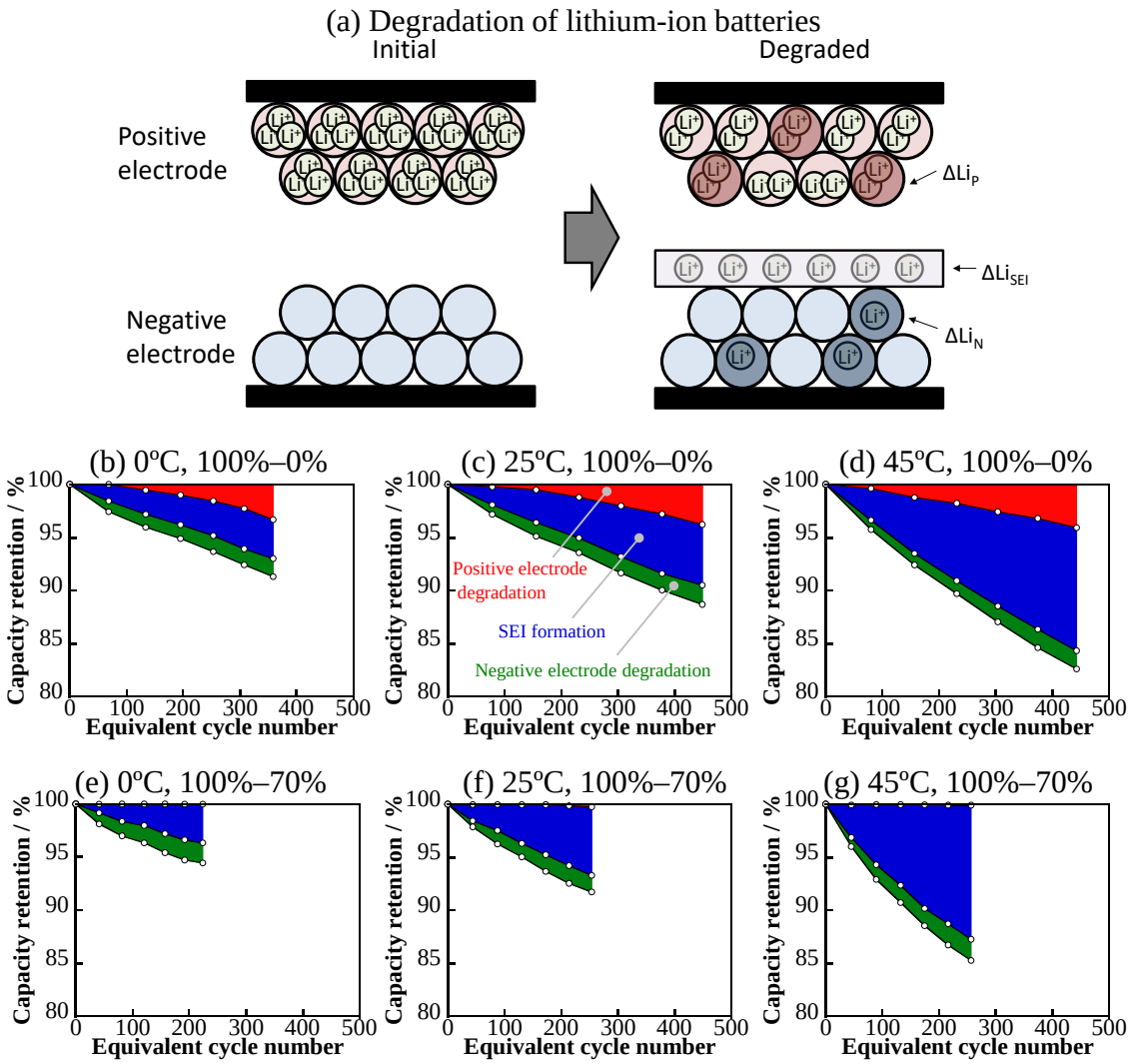

Figure 12. Degradation of lithium-ion batteries based on the estimation of active lithium ions (a), and changes in the degradation factors of the cells at (b) 0 °C and 100%–0%, (c) 25 °C and 100%–0%, (d) 45 °C and 100%–0%, (e) 0 °C and 100%–70%, (f) 25 °C and 100%–70%, and (g) 45 °C and 100%–70% estimated from the dV/dQ curve analysis.

Chapter 4.

Degradation Analysis of $LiNi_{0.8}Co_{0.15}Al_{0.05}O_2$ for Positive electrode Material of Lithium-Ion Battery Using Single-Particle Measurement

4-1. Introduction

Lithium-ion batteries (LIBs) have been extensively used in small electronic equipment such as mobile phones and laptops. Recently, they have also been used in electrically driven vehicles (xEVs) such as battery electric vehicles (BEVs) and plug-in hybrid electric vehicles (PHEVs). It is well-known that the degradation of LIBs, i.e., reduction in capacity and power, occurs after repeated charge/discharge and storage.[1, 2] I performed cycle life and storage life tests on LIBs under various conditions and reported that the degradation factors are mainly related to solid electrolyte interphase (SEI) formation and positive electrode degradation.[3, 4] It is known that the electrolyte solution is reduced at the negative electrode. The reduction products are deposited on the negative electrode to form the SEI.[5, 6] In this process, electricity is mainly consumed during charging by the extraction of Li^+ ions from the positive electrode. It is also consumed by both the SEI formation and the Li^+ ion-intercalation in the negative

electrode. This causes differences between the state-of-charge (SOC) of the negative electrode and that of the positive electrode.[7, 8]

Positive electrode degradation has been explained by the degradation of both the active materials as well as the electrode structures. An irreversible structural change from the layered structure of the parent phase to the rock-salt structure has been reported in the outermost surface of the particle for layered compounds such as $LiCoO_2$, $LiNi_{1-x-y}Co_xMn_yO_2$, and $LiNi_{1-x-y}Co_xAl_yO_2$ based on both transmission electron microscopy and X-ray absorption spectroscopy analyses methods.[9-11] Additionally, microcracks occurring in the secondary particles of the active materials have also been observed using the scanning electron microscopy (SEM) images.[10-12] In the case of Mn-based spinel compounds ($LiMn_{2-x}M_xO_4$), it has been reported that Mn^{3+} in the crystal structure dissolves in the electrolyte solution at a high temperature, which causes the degradation of $LiMn_{2-x}M_xO4$ (M = Mg, Al, etc.).[13, 14] The degradation of electrode structures, involving electronic disconnection between the active materials and loss of conductive carbon networks or current collectors, has been considered.[15-19] Typically, when the electrochemical characteristics of an active material are measured, cells are assembled with a composite electrode that contains binder, conducting materials, and active material. The binder and the conducting materials in the composite

electrode strongly influence the electrochemical characteristics of the active material. These are also influenced by the electrode structure, including its thickness and porosity.[20-23] Therefore, even when positive electrode degradation is detected in the coin-type half-cells, it is difficult to distinguish between the degradation of the active material and electrochemical degradation of the electrode structure.

A single particle measurement technique has been developed by Dokko et al. as a new technology for evaluating the electrochemical performance of one particle (5-40 μm in diameter) of the active material.[24] In the single particle measurement technique, electrochemical measurement of active materials can be achieved without using binder and conducting materials. Using this technique, the electrochemical reaction occurs according to the following three steps: (I) Diffusion of Li^+ between the particle surface and a bulk electrolyte solution, (II) transfer of Li^+ at the particle/electrolyte solution interface, and (III) Li^+ diffusion in the particle.[25] Generally, beause diffusion in the bulk electrolyte solution is faster than that caused in the particle due to the small current, the single particle electrochemical reaction rate is observed to be dependent on steps (II) or (III). The total process can be simplified by comparing with the case of the composite electrode.

Kanamura et al. performed single particle measurements on $LiCoO_2$, $LiFePO_4$,

$LiNi_{0.5}Mn_{1.5}O_4$, graphite, and SiCN and reported the electrochemical parameters (i.e., exchange current density, charge transfer reaction resistance, and solid phase diffusion coefficient) of these materials.[25–29] However, all these reports are initial performance evaluations, and there are no reports on the evaluation of degraded materials.

In this study, scanning transmission electron microscopy (STEM) observations and single particle measurements were conducted on $LiNi_{0.8}Co_{0.15}Al_{0.05}O_2$ before and after cycle testing to clarify the relations between structural changes in the active materials and capacity and power reduction.

4-2. Experimental

4-2-1. Cycle tests

A commercially available lithium-ion cell (3.25 Ah) with a $LiNi_{0.8}Co_{0.15}Al_{0.05}O_2$ positive electrode was used for the charge/discharge cycle test. The cell was charged at a C/3 rate to 4.2 V in constant current and was further charged in constant voltage (CC-CV) mode. Further, it was discharged at a C/3 rate to reach 2.5 V in constant current (CC) mode at 45°C in the atmosphere. There were 10 min intervals after each charge and discharge step. A low current charge/discharge test at a C/20 rate of 25°C in the atmosphere was performed after every 50 cycles. Furthermore,

electrochemical impedance spectroscopy was performed at an SOC of 50% at 25°C in the atmosphere, with an alternating current excitation of ±5 mV over the frequency range of 10 mHz–20 kHz after every 100 cycles.

4-2-2. Analysis of electrode

The three cells (uncycled, cycled 400 times, and cycled 800 times) were opened, and both the positive electrode and negative electrode were eliminated and washed using dimethyl carbonate (DMC). The electrodes were analyzed as follows.

The metal contents in the positive electrode were measured using inductively coupled plasma atomic emission spectrometer (ICP-AES, SPECTRO CIROS CCD, Spectro).

The electrochemical properties of the disassembled composite electrodes were investigated using 2032 coin-type cells. The coin cells were assembled using the disassembled negative electrode or positive electrode as the working electrode, lithium foil (Honjo Metal) as the counter electrode, and a mixed solvent of ethylene carbonate (EC) and diethyl carbonate (DEC) (1:1 in volume) containing 1 mol dm^{-3} lithium hexafluorophosphate ($LiPF_6$) (Kishida Chemical) as an electrolyte solution. Charge/discharge tests on the negative electrode and positive electrode half cells were

performed in the potential ranges of 0.005–0.15 V vs. Li/Li^+ at a C/20 rate and 4.3–2.5 V vs. Li/Li^+ at a C/50 rate at 25°C in the atmosphere.

The cross sections of the positive electrodes, prepared using an ion-milling system (IM4000 model, Hitachi High-Technologies), were observed using a field emission-scanning electron microscope (FE-SEM, S8020 model, Hitachi High-Technologies). Further, the particles of positive electrode-active material, which were obtained by washing the composite positive electrode with N-methyl-2-pyrrolidone (NMP, Kanto chemical) to eliminate the additives, i.e., polyvinylidene difluoride and conducting carbon, were also observed.

STEM was performed using a Cs-corrected STEM (JEM-ARM200F model, JEOL) that was operated at 200 kV. Uniform thin samples for STEM were prepared using a focused ion beam (FIB-SEM, SMF2000 model, Hitachi High-Technologies).

4-2-3. Single particle measurement

The particles of positive electrode-active material were also investigated by single particle measurement. A microprobe current collector, comprising an Au wire with a diameter of 10 μm surrounded by a borosilicate glass capillary, was used in the single particle measurement cell. The detailed fabrication method for the microprobe

current collector has been reported elsewhere.[30] The particles were spread on a glass filter paper. Further, the microprobe current collector was placed in contact with the target particle under an optical microscope using a micromanipulator. A piece of lithium metal foil (Honjo Metal) was the counter electrode, and a mixed solvent of EC and propylene carbonate (PC) (1:1 in volume) containing 1 mol dm^{-3} of lithium perchlorate ($LiClO_4$) (Kishida Chemical) was the electrolytic solution. Charge/discharge tests on the single particle were performed using an electrochemical analyzer (IviumStat model, Ivium) in the potential range of 4.3–2.5 V vs. Li/Li^+. Initially, the particle was charged and discharged at 7 nA in CC mode for three cycles. The charging current was maintained at 5 nA to ensure complete charging. However, the discharge current was increased from 5 to 40 nA during subsequent cycles. All the single particle measurements were performed in a glovebox filled with Ar gas at room temperature (around 25°C).

4-3. Results and discussion

4-3-1. Cycle life tests

Figure 1 (a) illustrates the capacity retention measured at 25°C during cycle life testing. The capacity decreased almost linearly up to 800 cycles. The capacity retention

was approximately 76% at 400 cycles and approximately 54% at 800 cycles. Figure 1 (b) depicts the AC impedance spectra that were measured after every 100 cycles. The impedance spectra revealed two distinct semicircles. The semicircle in the lower frequency region considerably increased with the number of cycles. Figure 1 (c) depicts the change in each resistance estimated by fitting impedance data using the equivalent circuit that is illustrated in Figure 1 (b). In general, R_0 represents the ohmic resistance, including the Li^+ diffusion in the electrolyte, whereas R_1 in the higher frequency region represents the charge transfer resistance of the negative electrode, and R_2 in the lower frequency region represents the charge transfer resistance of the positive electrode.[31, 32] R_0 increased during the initial 400 cycles, whereas R_1 hardly increased. It is considered that R_0 increased due to a decrease the amount of the electrolyte and/or the growth of SEI, which is caused by the decomposition of organic solutions and $LiPF_6$ during the cycle test. However, R_2 increased slightly during the initial 400 cycles and increased drastically during 400–800 cycles. These results indicate that the degradation mode altered at approximately 400 cycles; therefore, the three cells were disassembled, uncycled, cycled 400 times, and cycled 800 times. Further, the collected electrodes were analyzed.

4-3-2. Analysis of electrode

The ICP-AES analysis result shows that the positive electrode comprises nickel, cobalt, and aluminum as the basic metals, with a ratio of 80:15:5 (Ni:Co:Al).

The charge/discharge curves of half cells using the electrodes (negative electrode and positive electrode) that were obtained by disassembling the cells (uncycled, cycled 400 times, and cycled 800 times) are depicted in Figure 2. The solid and dotted lines represent the first and second cycles, respectively. The negative electrode half cells were initiated from the discharge process (insertion of Li^+), and the positive electrode half cells were initiated from the charge process (desorption of Li^+). The shapes of the charge/discharge curves of the negative electrode before and after the cycle test and the capacity of the negative electrode remained constant, indicating that the negative electrode did not degrade. However, the shapes of the charge/discharge curves of the positive electrodes altered significantly. In the uncycled positive electrode, the initial charge capacity was smaller than the discharge capacity, which indicated that the positive electrode was not completely discharged in the 18650 full cell.[7] This phenomenon suggests that the reaction regions of the positive electrode and negative electrode were different, and the positive electrode and negative electrode had been operated in different SOC regions in the 18650 full cell. For the positive electrode that

was cycled 400 times, the capacity difference between the first charge and discharge capacities became larger than that of the uncycled positive electrode, which caused larger different SOC regions for the positive electrode and negative electrode. The discharge capacity of the positive electrode decreased to 86% as compared with that of the uncycled positive electrode during the initial 400 cycles. Furthermore, the discharge capacity of the positive electrode decreased nonlinearly to 45% as compared with that of the uncycled positive electrode during 800 cycles. The difference between the charge and discharge capacities for the positive electrode that was cycled 800 times disappeared. These phenomena may be caused due to the consumption of Li^+ ions by SEI-formation during initial 400 cycles and the rapid degradation of the positive electrode from 400 to 800 cycles. The degradation of the positive electrode-active materials was investigated using SEM, STEM, and single particle measurement.

SEM images of the positive electrode cross sections and a particle of positive electrode-active material, which was collected by washing with NMP and DMC to eliminate the binder and the conductive material, are depicted in Figure 3. The SEM images indicated that the particle of the positive electrode-active material was a secondary particle depicting a diameter of approximately 20 μm, which was formed by the agglomeration of primary submicron particles. In this study, this secondary particle

was defined as a "single particle". No significant differences were confirmed between the uncycled particle and the particle that was cycled 400 times. For the particle that was cycled 800 times, microcracks were observed inside the secondary particles (the grain boundaries between primary particles).

STEM was used to observe four locations at the surface and inside the exterior primary particle and at the surface and inside the interior primary particle. Figure 4 depicts the representative STEM images (high-angle annular dark field (HAADF) images) of the surfaces of the exterior primary particles. HAADF-STEM images were captured along the [100] or [110] zone axes in $LiNi_{0.8}Co_{0.15}Al_{0.05}O_2$ to depict the $R\bar{3}m$ layered structure. The influence for active materials by electron beam was not observed. In the uncycled particle that is depicted in Figure 4 (a), the layered structure was observed except the uppermost surface layer. Figures 4 (A) and (B) depict fast Fourier transform (FFT) patterns of the regions A and B that are surrounded by red frames in Figure 4 (a). These regions were potentially identified as the (100) face of $R\bar{3}m$.

In the particles that were cycled 400 times, as depicted in Figure 4 (b), a layered structure was confirmed inside the primary particle. Additionally, high contrast spots were confirmed in the Li layer around the surface, corresponding to the structural changes (formation of decomposition phase). Figures 4 (C) and (D) depict the FFT

patterns of regions C and D that were surrounded by red frames in Figure 4 (b). Region D was potentially indexed to the (110) face of $R\bar{3}m$. However, in Region C, some spots were different from those that were observed in Region D. This phenomenon suggested that the structure altered to a cubic crystal, corresponding to the rock salt-type NiO-like structure ($Fm\bar{3}m$).[11] This behavior is consistent with the literature[33]. The surface decomposition phase was approximately 8 nm thick. Subsequently, in the particle. 800 times as depicted in Figure 4 (c), a decomposition phase similar to that of the particles that were cycled 400 times was confirmed on the outermost surface. The electron energy loss spectroscopy (EELS) spectra of the exterior primary particle were shown in Figure 5. At around 8 nm on the surface of the particles that were cycled 400 and 800 times, the shifts of Ni L_3 peak for low energy were observed. This suggests that $LiNiO_2$-like structure changed to NiO-like structure.

Figure 6 depicts the representative STEM images (HAADF images) of the surfaces of interior primary particles. The uncycled particle depicted in Figure 6 (a) had a uniform layer structure similar to that depicted in Figure 4 (a). The particle cycled 400 times that was illustrated in Figure 6 (b) had a uniform layer structure except near the surface (~3 nm) where a migration of transition metal ions (Ni or Co) to the Li layer was confirmed, and it was suggested that there was a slight formation of the cubic

rock-salttype NiO-like structure. Even in the particle cycled 800 times that is depicted in Figure 6 (c), surface alteration was confirmed, and the thickness was the same or slightly thicker than one of the particles cycled 400 times. Interestingly, inside the internal primary particles that were cycled 800 times, a high contrast image was observed in the Li layer framed by a broken line in Figure 6 (c), as depicted by the single-headed arrows. This region exhibited an island morphology. Namely, a degradation phase was also formed inside the primary particle. This suggests that the transition metal ions (Ni or Co) migrate to the Li layer due to long-term charge/discharge, even inside the particles that are not directly in contact with the electrolyte solution, and the structure changes to rock salt-type.

The relations between the location and structure confirmed by STEM are summarized in Table 1. The uncycled particle had a uniform layered structure. However, structural changes were confirmed on the outermost surface of the particle that was cycled 400 times. In the particle that was cycled 800 times, a structural change was confirmed inside the primary particle at the outermost surface. The influence of the structural changes in the active material particles on the electrochemical properties were investigated using single particle measurement.

4-3-3. Single particle measurement

Figure 7 depicts the discharge curves of each collected single particle measured at various discharge currents from 0.5 to 40 nA. From the optical microscopy observations, the particle diameters of each measured single particle were both observed to be approximately 18 μm. The theoretical capacity of the single particle was estimated to be 1.47 nA h using 160 mA h g^{-1} as the actual capacity and 3 g cm^{-3} as the consolidated density. In the uncycled single particle, 0.5 nA corresponds to a rate of about 0.3 C (discharge time 10324 s), and 40 nA corresponds to a rate of about 28 C (discharge time 96 s). The capacity retention at 40 nA against 0.5 nA is 76%. For the single particle cycled 400 times, the capacity retention at 40 nA against 0.5 nA is 72%, which is almost the same as that of the uncycled particle. The overpotential of the particle cycled 400 times was larger than that of the uncycled one. For the particle cycled 800 times, the capacity retention at 40 nA against 0.5 nA was 25%. Compared with the particle cycled 400 times, the capacity retention decreased and the polarization increased.

To estimate the exchange current density and apparent diffusion coefficient of Li^+ in the secondary particle, I drew quasi Tafel plots from each discharge curve at a depth of discharge (DOD) of 10%, which is depicted by the dotted lines in Figure 7

From the quasi Tafel plot of the uncycled particle in Figure 8 (a), three regions were confirmed. Region I depicted a current between 2 and 5 nA. The overpotentials were sufficiently large, and this behaved according to the Tafel equation (equation (1)).[34] The measured points formed a straight line with a slope of $-\alpha F/2.3RT$ (= Tafel line).

$$\log i = \log i_0 - \frac{\alpha F}{2.303RT}(E - E_{\mathrm{eq}}) \quad (1)$$

Here, i is the applied current density normalized by a surface area of the single particle which is assumed to be a sphere, i_0 is the exchange current density, α is the transfer coefficient (typically assumed to be 0.5[35, 36]), F is the Faraday constant, R is the gas constant, T is the temperature, E_{eq} is the equilibrium potential, and E is the measured potential. The E_{eq} for a DOD of 10% was calculated by taking the midpotential between the potential at an SOC of 90% during charging at 0.5 nA and the potential at a DOD of 10% during discharging at 0.5 nA.[37] The i_0 of the uncycled particle was estimated to be 1.5×10^{-1} mA cm^{-2} by fitting the straight line of Region I using the Tafel equation and extrapolating it to an E_{eq} of 4.16 V vs. Li/Li$^+$. α in the Tafel equation was determined 0.5 from the symmetry of reactions between the discharge process and the charge process of the positive electrode (Figure 9). The charge transfer resistance (R_{ct}) was calculated to be 0.2×10^3 Ω cm^2 using equation (2) and i_0.[34]

$$R_{\mathrm{ct}} = \frac{RT}{Fi_0} \quad (2)$$

Region II depicts a current of 10 nA or more. The measurement point deviates from the Tafel

line since the rate-determining step of the reaction processes has changed from step (II) to step (III). The apparent diffusion coefficient in the particle can be estimated as 2.0×10^{-10} cm^2 s^{-1} according to equation (3)[38] with the particle radius and discharge time at the minimum current value in region II.

$$D = \frac{L^2}{6t} \quad (3)$$

Here, D is the diffusion coefficient, L is the diffusion length of Li^+ in the secondary particle, which is considered to be the same as the secondary particle radius, and t is the diffusion time that is required to almost completely discharge the secondary particle.

Region III depicts a current of 2 nA or less. Further, the plots deviate sharply from linear behavior as the potential approaches E_{eq} because the back reaction can no longer be considered to be negligible.[34]

This calculation method may be have an error due to taking a logarithmic scale in quasi Tafel plots. However, this method is probably accurate to calculate the exchange current density and the apparent diffusion coefficient, because those values of the uncycled $LiNi_{0.8}Co_{0.15}Al_{0.05}O_2$ particle are almost same with the values calculated by EIS measurements[35] and simulations[36].

The exchange current density and apparent diffusion coefficient in the particle cycled 400 times and the particle cycled 800 times were determined using the same procedure and are presented in Table 2. However, for the particle cycled 800 times, the Tafel line was not observed within the measured current range. In this study, the exchange current density and the apparent diffusion coefficient of the particle cycled 800 times were estimated using the following approaches. The exchange current density was considered to be 0.01×10^{-1} to 0.05×10^{-1} mA cm^{-2}, which was estimated by drawing the Tafel line through the point at 0.5 nA and extrapolating it to E_{eq} (point a in Figure 8 (c)) and by fitting a straight line of region II and extrapolating it to E_{eq} (point b in Figure 8 (c)), respectively. The apparent diffusion coefficient in the particle was estimated to be 0.2×10^{-10} cm^2 s^{-1} or less that estimated from the discharge time at 0.5 nA.

Using the alteration in the exchange current density and the apparent diffusion coefficient in the particle, it is concluded that the exchange current density dramatically decreases during the initial 400 cycles and that the apparent diffusion coefficient is considerably reduced from 400 to 800 cycles. It can be assumed that these phenomena are caused due to the structural changes observed by STEM. A schematic of the degradation of a $LiNi_{0.8}Co_{0.15}Al_{0.05}O_2$ particle during cycling is depicted in Figure 10. As observed in the particle cycled 400 times, the decomposition phase was formed at

the outermost surface of the secondary particle during the initial 400 cycles. This decomposition phase hinders the insertion/desorption of Li^+ at the active material/electrolyte solution interface, which causes a decrease in exchange current density (increase in charge transfer resistance). As observed in the particle cycled 800 times, the decomposition phase inside the particle was formed from 400 to 800 cycles. This decomposition phase hinders the diffusion of Li^+ inside the particle, which causes a decrease in the apparent diffusion coefficient of the particle.

4-4. Conclusion

In this study, to understand the influences of structural changes in positive electrode-active materials on electrochemical performance, cycle tests of commercial lithium-ion cells with $LiNi_{0.8}Co_{0.15}Al_{0.05}O_2$ positive electrodes were performed. Positive electrodes obtained from uncycled cells and the cells that were cycled 400 and 800 times were analyzed using STEM and single particle measurement. Before cycle testing, the uniform layered structure of the positive electrode material was confirmed. After 400 cycles, a NiO-like layer with an $Fm\bar{3}m$ structure was formed on the outermost surface of the particle. After 800 cycles, the NiO-like structure had formed not only on the outermost surface but also inside the particle. The rate capability of each

single positive electrode particle, which was obtained by washing the composite positive electrode to eliminate the additives, were measured to evaluate the exchange current density (i_0) and the apparent diffusion coefficient of Li^+ in the particle (D) using quasi Tafel plots. These phenomena are caused due to the structural changes observed by STEM. The decomposition phase was formed at the outermost surface of the secondary particles during the initial 400 cycles. This decomposition phase may hinder the insertion/desorption of Li^+ at the active material/electrolyte solution interface, which causes a decrease in the exchange current density (increase in the charge transfer resistance). The decomposition phase inside the particle was formed from 400 to 800 cycles. This decomposition phase also hinders the diffusion of Li^+ inside the particle, which causes a decrease in the apparent diffusion coefficient of the particle.

These results clarify both electrochemically and quantitatively that the structural changes in the outermost surface hinder the insertion/desorption of Li^+ ions at the active material/electrolyte interface and that the structural changes inside the particle also hinder the diffusion of Li^+ ions in the particle. Because the change in crystal structure leads to an increase in the internal resistance, to realize long-life layered positive electrode materials, it was clearly revealed that it is important to suppress the cation mixing of the transition metals (TM) into the Li layer from the TM layer.

References

[1] T. Matsuda, M. Myojin, K. Ando, D. Imamura, Degradation Analyses of Commercial Lithium-Ion Cells by Temperature/C-rate Controlled Cycle Test, ECS Trans. 64 (2015) 69–75. DOI: 10.1149/06422.0069ecst

[2] M. Ecker, N. Nieto, S. Käbitz, J. Schmalstieg, H. Blanke, A. Warnecke, D.U. Sauer, Calendar and cycle life study of Li(NiMnCo)O_2-based 18650 lithium-ion batteries. J. Power Sources, 248 (2014) 839–851. DOI: 10.1016/j.jpowsour.2013.09.143

[3] K. Ando, T. Matsuda, D. Imamura, Degradation Diagnosis of Lithium-ion Batteries with a $LiNi_{0.5}Co_{0.2}Mn_{0.3}O_2$ and $LiMn_2O_4$ Blended Cathode Using dV/dQ Curve Analysis. J. Power Sources, 390 (2018) 278–285. DOI: 10.1016/j.jpowsour.2018.04.043

[4] K. Ando, T. Matsuda, M. Myojin, D. Imamura, Calendar Degradation Mechanism of Lithium Ion Batteries with a $LiMn_2O_4$ and $LiNi_{0.5}Co_{0.2}Mn_{0.3}O_2$ Blended Cathode. ECS Trans. 75 (2017) 77–90. DOI: 10.1149/07523.0077ecst

[5] V. A. Agubra, J. W. Fergus, The formation and stability of the solid electrolyte interface on the graphite anode. J. Power Sources, 268 (2014) 153–162. DOI: 10.1016/j.jpowsour.2014.06.024

[6] S.-H. Lee, H.-G. You, K.-S. Han, J. Kim, I.-H. Jung, J.-H. Song, A new approach to surface properties of solid electrolyte interphase on a graphite negative electrode. J. Power Sources, 247 (2014) 307–313. DOI: 10.1016/j.jpowsour.2013.08.105

[7] K. Shono, T. Kobayashi, M. Tabuchi, Y. Ohno, H. Miyashiro, Y. Kobayashi, Proposal of simple and novel method of capacity fading analysis using pseudo-reference electrode in lithium ion cells: Application to solvent-free lithium ion polymer batteries. J. Power Sources, 247 (2014) 1026–1032. DOI: 10.1016/j.jpowsour.2013.06.071

[8] K. Honkura, T. Horiba, Study of the deterioration mechanism of $LiCoO_2$/graphite cells in charge/discharge cycles using the discharge curve analysis. J. Power Sources, 264 (2014) 140–146. DOI: 10.1016/j.jpowsour.2014.04.036

[9] F. Lin, I.M. Markus, D. Nordlund, T.-C. Weng, M.D. Asta, H.L. Xin, M.M. Doeff, Surface reconstruction and chemical evolution of stoichiometric layered cathode materials for lithium-ion batteries. Nat. Commun. 5 (2014) 3529–3537. DOI: 10.1038/ncomms4529

[10] H.-H. Sun, A. Manthiram, A. Impact of Microcrack Generation and Surface Degradation on a Nickel-Rich Layered $Li[Ni_{0.9}Co_{0.05}Mn_{0.05}]O_2$ Cathode for

Lithium-Ion Batteries. Chem. Mater. 29 (2017) 8486–8493. DOI: 10.1021/acs.chemmater.7b03268

[11] S. Watanabe, M. Kinoshita, T. Hosokawa, K. Morigaki, K. Nakura, Capacity fading of $LiAl_yNi_{1-x-y}Co_xO_2$ cathode for lithium-ion batteries during accelerated calendar and cycle life tests (effect of depth of discharge in charge–discharge cycling on the suppression of the micro-crack generation of $LiAl_yNi_{1-x-y}Co_xO_2$ particle). J. Power Sources, 260 (2014) 50–56. DOI: 10.1016/j.jpowsour.2014.02.103

[12] A. O. Kondrakov, A. Schmidt, J. Xu, H. Geβwein, R. Monig, P. Hartmann, H. Sommer, T. Brezesinski, J. Janek, Anisotropic Lattice Strain and Mechanical Degradation of High- and Low-Nickel NCM Cathode Materials for Li-Ion Batteries. J. Phys. Chem. C. 121 (2017) 3286−3294. DOI: 10.1021/acs.jpcc.6b12885

[13] Y. Nishi, Lithium ion secondary batteries; past 10 years and the future. J. Power Sources, 100 (2001) 101–106. DOI: 10.1016/S0378-7753(01)00887-4

[14] N.-S. Choi, J.-T. Yeon, Y.-W. Lee, J.-G. Han, K. T. Lee, S.-S. Kim, Degradation of spinel lithium manganese oxides by low oxidation durability of $LiPF_6$-based electrolyte at 60 °C. Solid State Ionics, 219 (2012) 41–48. DOI: 10.1016/j.ssi.2012.05.012

[15] C. Wang, A.J. Appleby, F.E. Little, Electrochemical study on nano-Sn, $Li_{4.4}Sn$ and $AlSi_{0.1}$ powders used as secondary lithium battery anodes. J. Power Sources, 93 (2001) 174–185. DOI: 10.1016/S0378-7753(00)00576-0

[16] J.H. Ryu, J.W. Kim, Y.-E. Sung, S.M. Oh, Failure Modes of Silicon Powder Negative Electrode in Lithium Secondary Batteries. Electrochemical and Solid-State Letters, 7 (2004) A306–A309. DOI: 10.1149/1.1792242

[17] J. Vetter, P. Novák, M.R. Wagner, C.Veit, K.-C. Möller, J.O. Besenhard, M. Winter, M.W.-Mehrens, C. Vogler, Ageing mechanisms in lithium-ion batteries. J. Power Sources, 147 (2005) 269–281. DOI: 10.1016/j.jpowsour.2005.01.006

[18] T. Waldmann, A. Iturrondobeitia, M. Kasper, N. Ghanbari, F. Aguesse, E. Bekaert, L. Daniel, S. Genies, I.J. Gordon, M.W. Loble, E.D. Vito, M.W.-Mehrens, Disassembly Methodology and Physico-Chemical Analysis Techniques. J. Electrochem. Soc. 163 (2016) A2149–A2164. DOI: 10.1149/2.1211609jes

[19] Y. Merla, B. Wu, V. Yufit, N.P. Brandon, R.F. Martinez-Botas, G.J. Offer, Novel application of differential thermal voltammetry as an in-depth state-of-health diagnosis method for lithium-ion batteries. J. Power Sources, 307 (2016) 308–319. DOI: 10.1016/j.jpowsour.2015.12.122

[20] D. E. Stephenson, E. M. Hartman, J. N. Harb, D. R. Wheeler, Modeling of Particle-Particle Interactions in Porous Cathodes for Lithium-Ion Batteries. J. Electrochem. Soc. 154 (2007) A1146–A1155. DOI: 10.1149/1.2783772

[21] J. Newman, K.E. Thomas-Alyea, Electrochemical Systems, third ed.; John Wiley & Sons Inc.: Hoboken, NJ (2004). ISBN: 978-0-471-47756-3

[22] M. Katayama, K. Sumiwaka, K. Hayashi, K. Ozutsumi, T. Ohta, Y. Inada, Inada, Y. Development of a two-dimensional imaging system of X-ray absorption fine structure. J. Synchrotron Radiat, 19 (2012) 717–721. DOI: 10.1107/S0909049512028282

[23] K. Suzuki, B. Barbiellini, Y. Orikasa, S. Kaprzyk, M. Itou, K. Yamamoto, Y. J. Wang, H. Hafiz, Y. Uchimoto, A. Bansil, Y. Sakurai, and H. Sakurai, Non-destructive measurement of in-operando lithium concentration in batteries via x-ray Compton scattering. J. Appl. Phys. 119 (2016) 025103. DOI: 10.1063/1.4939304

[24] K. Dokko, M. Mohamedi, Y. Fujita, T. Itoh, M. Nishizawa, M. Umeda, I. Uchida, Kinetic Characterization of Single Particles of $LiCoO_2$ by AC Impedance and Potential Step Methods. J. Electrochem. Soc. 148 (2001) A422–A426. DOI: 10.1149/1.1359197

[25] H. Munakata, B. Takemura, T. Saito, K. Kanamura, Evaluation of real performance of $LiFePO_4$ by using single particle technique. J. Power Sources, 217 (2012) 444–448. DOI: 10.1016/j.jpowsour.2012.06.037

[26] K. Dokko, N. Nakata, K. Kanamura, High rate discharge capability of single particle electrode of $LiCoO_2$. J. Power Sources, 189 (2009) 783–785. DOI: 10.1016/j.jpowsour.2008.07.081

[27] K. Nishikawa, N. Zettsu, K. Teshima, K. Kanamura, Intrinsic electrochemical characteristics of one $LiNi_{0.5}Mn_{1.5}O_4$ spinel particle. J. Electroanalytical Chemistry, 799 (2017) 468–472. DOI: 10.1016/j.jelechem.2017.06.042

[28] S. Lim, J.-H. Kim, Y. Yamada, H. Munakata, Y.-S. Lee, S.-S. Kim, K. Kanamura, Improvement of rate capability by graphite foam anode for Li secondary batteries. J. Power Sources, 355 (2017) 164–170. DOI: 10.1016/j.jpowsour.2017.04.047

[29] L. M. Reinold, Y. Yamada, M. G.-Zaja, H. Munakata, K. Kanamura, Riedel, R. The influence of the pyrolysis temperature on the electrochemical behavior of carbon-rich SiCN polymer-derived ceramics as anode materials in lithium-ion batteries. J. Power Sources, 282 (2015) 409–415. DOI: 10.1016/j.jpowsour.2015.02.074

[30] H. Shiku, T. Takeda, H. Yamada, T. Matsue, I. Uchida, Microfabrication and Characterization of Diaphrase-Patterned Surfaces by Scanning Electrochemical Microscopy. Anal. Chem. 67 (1995) 312–317. DOI: 10.1021/ac00098a014

[31] D. Zhang, B.S. Haran, A. Durairajan, R.E. Whit , Y. Podrazhansky, B.N. Popov, Studies on capacity fade of lithium-ion batteries. J. Power Sources, 91 (2000) 122–129. DOI: 10.1016/S0378-7753(00)00469-9

[32] T. Momma, M. Matsunaga, D. Mukoyama, T. Osaka, T. Ac impedance analysis of lithium ion battery under temperature control. J. Power Sources, 216 (2012) 304–307. DOI: 10.1016/j.jpowsour.2012.05.095

[33] S. Zheng, R. Huang, Y. Makimura, Y. Ukyo, C. A. J. Fisher, T. Hirayama, Y. Ikuhara, Microstructural Changes in $LiNi_{0.8}Co_{0.15}Al_{0.05}O_2$ Positive Electrode Material during the First Cycle. J. Electrochem Soc. 158 (2011) A357–A362. DOI: 10.1149/1.3544843

[34] A. J. Bard, L. R. Faulkner, Electrochemical Methods; Fundamentals and Applications: John Wiley & Sons: New York, (1980) 87–106. ISBN: 978-0-471-04372-0

[35] P.-C. Tsai, B. Wen, M. Wolfman, M.-J. Choe, M. S. Pan, L. Su, K. Thornton, J. Cabana, Y.-M. Chiang, Single-particle measurements of electrochemical kinetics in NMC and NCA cathodes for Li-ion batteries. Energy & Environmental Science. 11 (2018) 860–871. DOI: 10.1039/c8ee00001h

[36] D.W. Dees, K.G. Gallagher, D.P. Abraham, A.N. Jansen, Electrochemical Modeling the Impedance of a Lithium-Ion Positive Electrode Single Particle. J. Electrochem. Soc. 160 (2013) A478–A486. DOI: 10.1149/2.055303jes

[37] K. Dokko, N. Nakata, Y. Suzuki, K. Kanamura, High-Rate Lithium Deintercalation from Lithiated Graphite Single-Particle Electrode. J. Phys. Chem. C. 114 (2010) 8646–8650. DOI: 10.1021/jp101166d

[38] H. C. Berg, Random Walks in Biology; Diffusion: Macroscopic Theory: Princeton University Press, (1993). SIBN: 978-0-691-00064-0

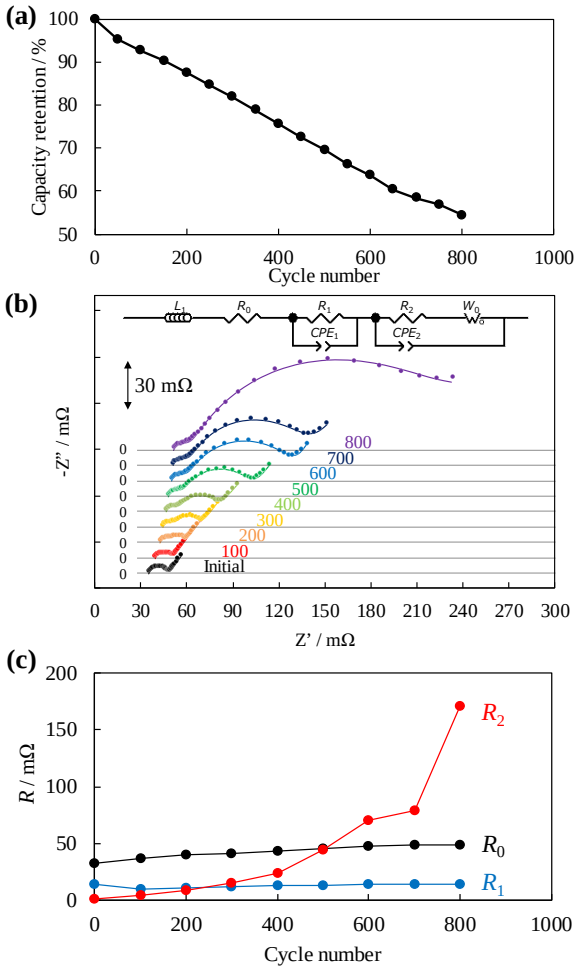

Figure 1. (a) Capacity retention and (b) impedance variations in LIB charge/discharge cycling measured at 25°C, and (c) resistance variations in LIB that was estimated by fitting for impedance in (b).

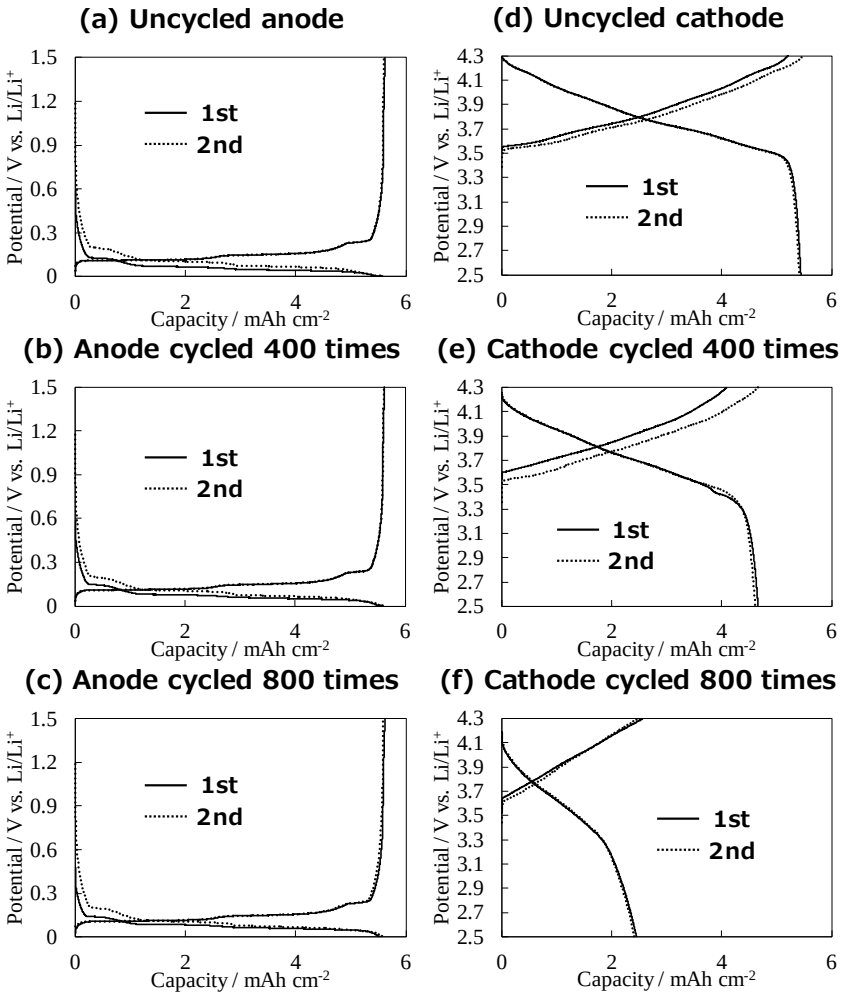

Figure 2. Charge and discharge curves of the half cell for (a) the uncycled negative electrode, (b) the negative electrode cycled 400 times, (c) the negative electrode cycled 800 times, (d) the uncycled positive electrode, (e) the positive electrode cycled 400 times, and (f) the positive electrode cycled 800 times. The solid and dotted lines represent the first and second cycles, respectively.

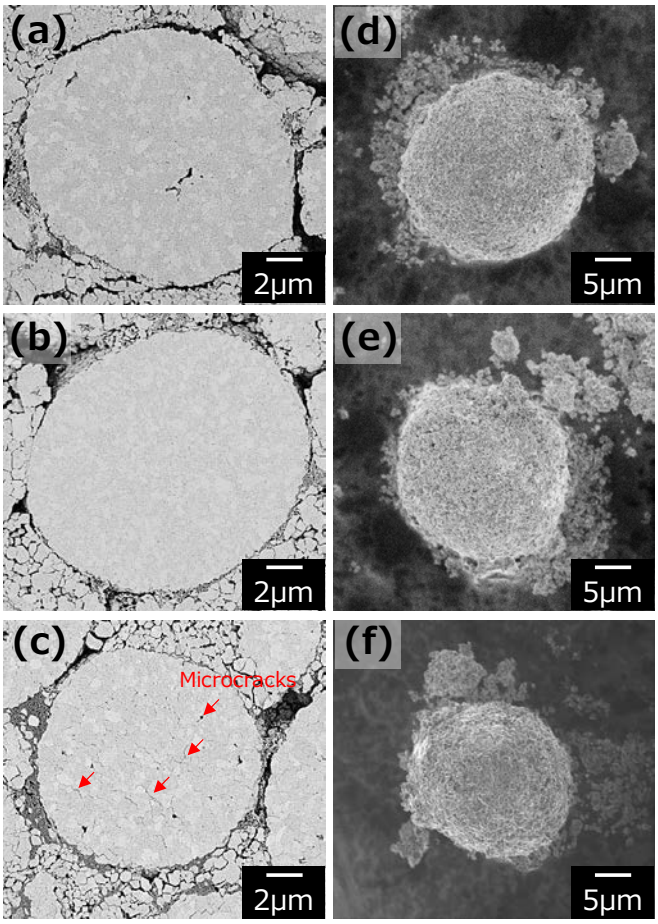

Figure 3. SEM images of (a) cross section of the uncycled positive electrode, (b) cross section of the positive electrode cycled 400 times, (c) cross section of the positive electrode cycled 800 times, (d) single particle of the uncycled positive electrode, (e) single particle of the positive electrode cycled 400 times, and (f) single particle of the positive electrode cycled 800 times.

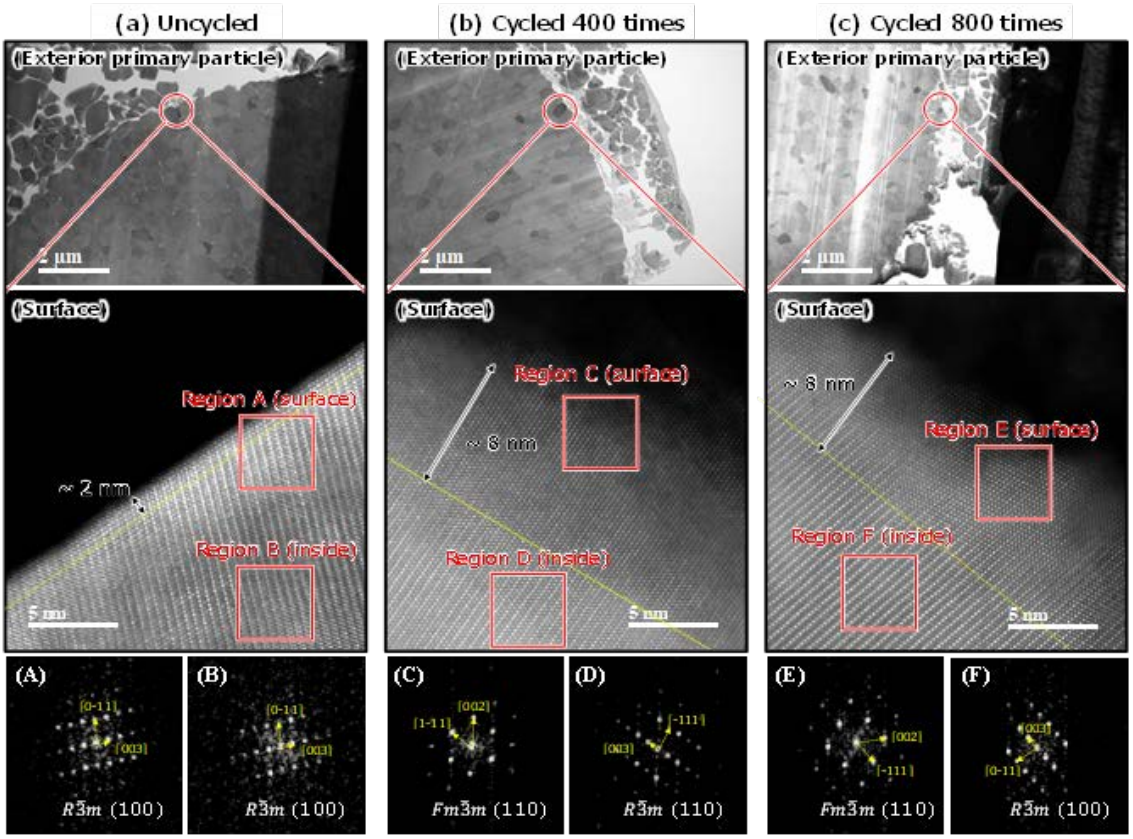

Figure 4. STEM images of the exterior primary particle of (a) an uncycled $LiNi_{0.8}Co_{0.15}Al_{0.05}O_2$ particle, (b) a $LiNi_{0.8}Co_{0.15}Al_{0.05}O_2$ particle cycled 400 times, and (c) a $LiNi_{0.8}Co_{0.15}Al_{0.05}Al_yO_2$ particle cycled 800 times. (A)–(F) depict the FFT patterns for each region.

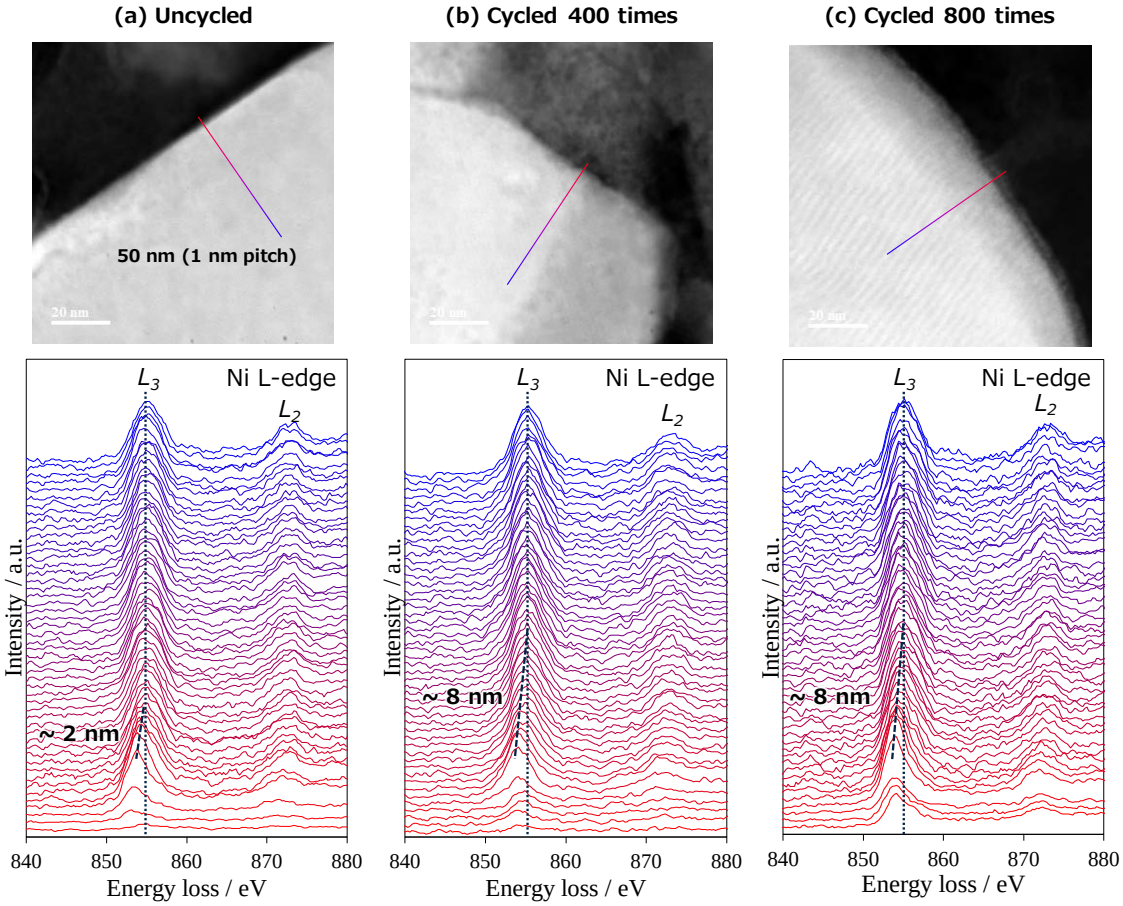

Figure 5. EELS spectra analysis of the exterior primary particle of (a) an uncycled $LiNi_{0.8}Co_{0.15}Al_{0.05}O_2$ particle, (b) a $LiNi_{0.8}Co_{0.15}Al_{0.05}O_2$ particle cycled 400 times, and (c) a $LiNi_{0.8}Co_{0.15}Al_{0.05}O_2$ particle cycled 800 times.

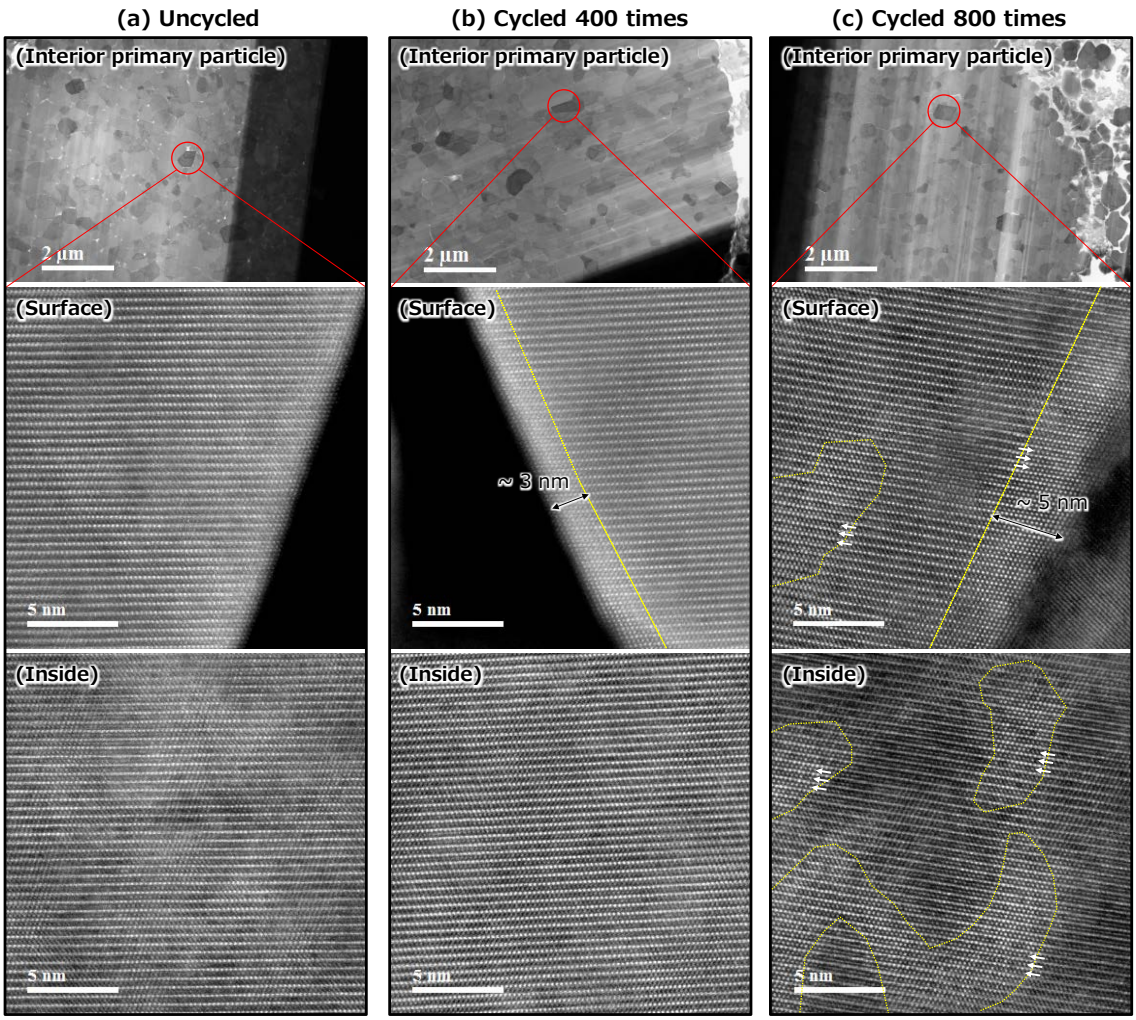

Figure 6. STEM images of the interior primary particles of (a) an uncycled $LiNi_{0.8}Co_{0.15}Al_{0.05}O_2$ particle, (b) a $LiNi_{0.8}Co_{0.15}Al_{0.05}O_2$ particle cycled 400 times, and (c) a $LiNi_{0.8}Co_{0.15}Al_{0.05}O_2$ particle cycled 800 times.

Table 1. Summary of STEM observation of $LiNi_{0.8}Co_{0.15}Al_{0.05}O_2$ particle before and after cycling.

Sample		Uncycled	Cycled 400 times	Cycled 800 times
Exterior primary particle	Surface	Layered	NiO type	NiO type
	Inside	Layered	Layered	Two-phase coexistence (Layered and NiO type)
Interior primary particle	Surface	Layered	Layered – NiO type	NiO type – Layered
	Inside	Layered	Layered	Two-phase coexistence (Layered and NiO type)

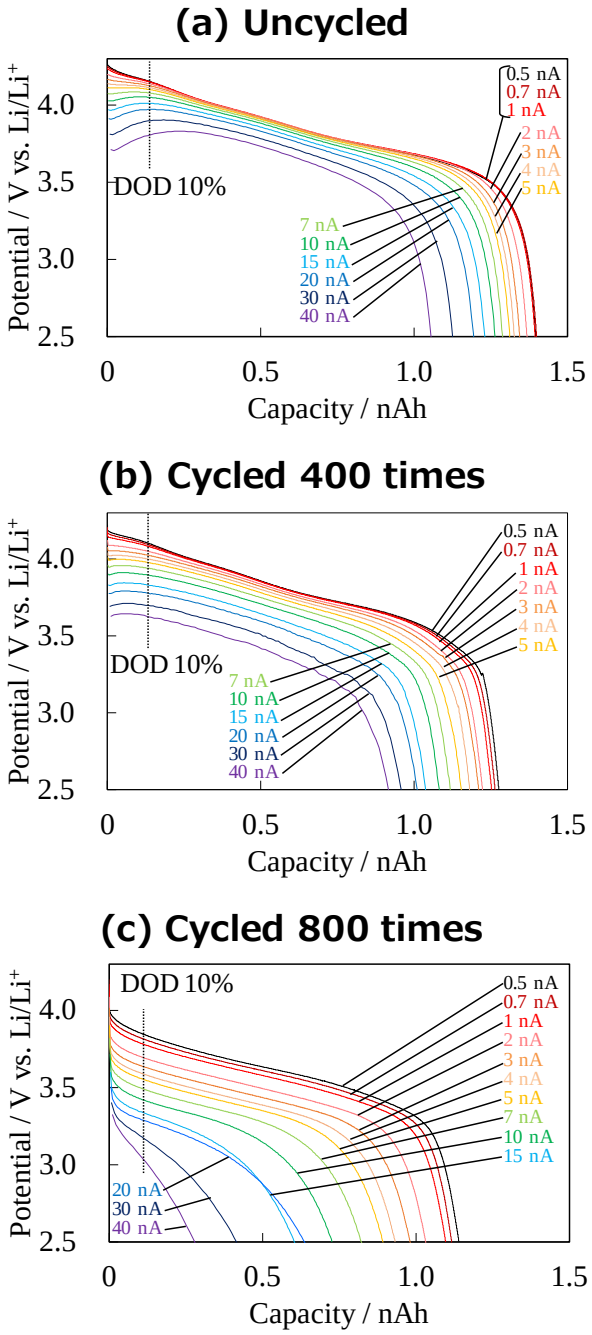

Figure 7. Discharge curves of (a) an uncycled $LiNi_{0.8}Co_{0.15}Al_{0.05}O_2$ particle, (b) a $LiNi_{0.8}Co_{0.15}Al_{0.05}O_2$ particle cycled 400 times, and (c) a $LiNi_{0.8}Co_{0.15}Al_{0.05}O_2$ particle cycled 800 times, which was measured at various currents from 0.5 to 40 nA.

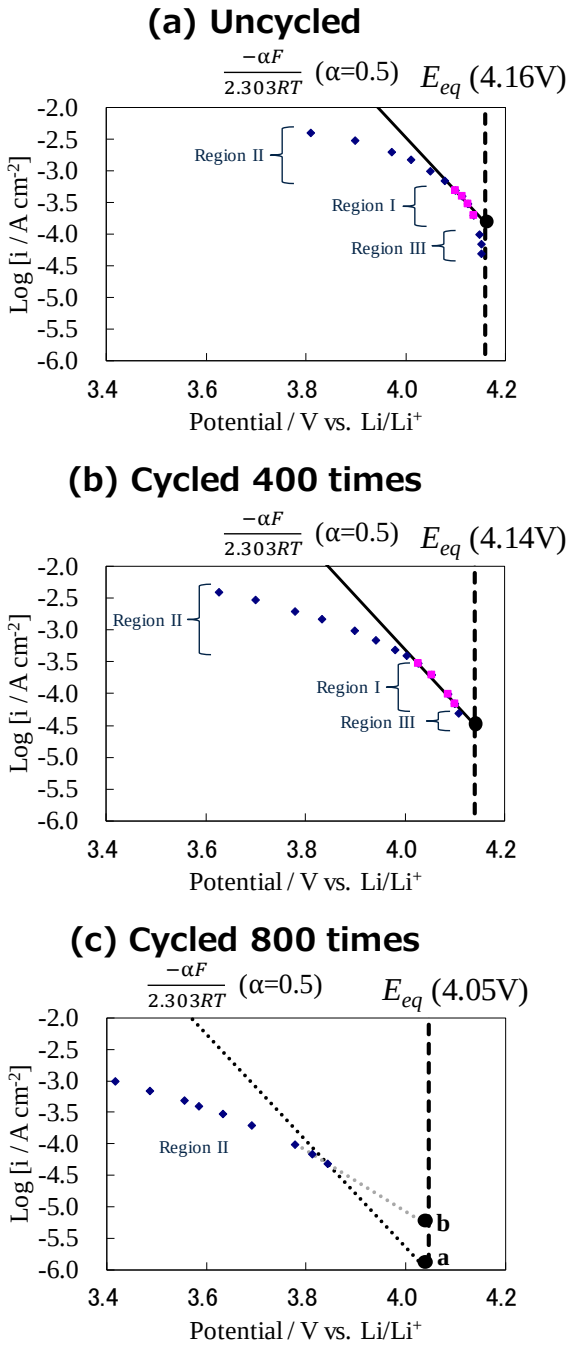

Figure 8. Quasi Tafel plots of (a) an uncycled $LiNi_{0.8}Co_{0.15}Al_{0.05}O_2$ particle, (b) a $LiNi_{0.8}Co_{0.15}Al_{0.05}O_2$ particle cycled 400 times, and (c) a $LiNi_{0.8}Co_{0.15}Al_{0.05}O_2$ particle cycled 800 times at a DOD of 10%.

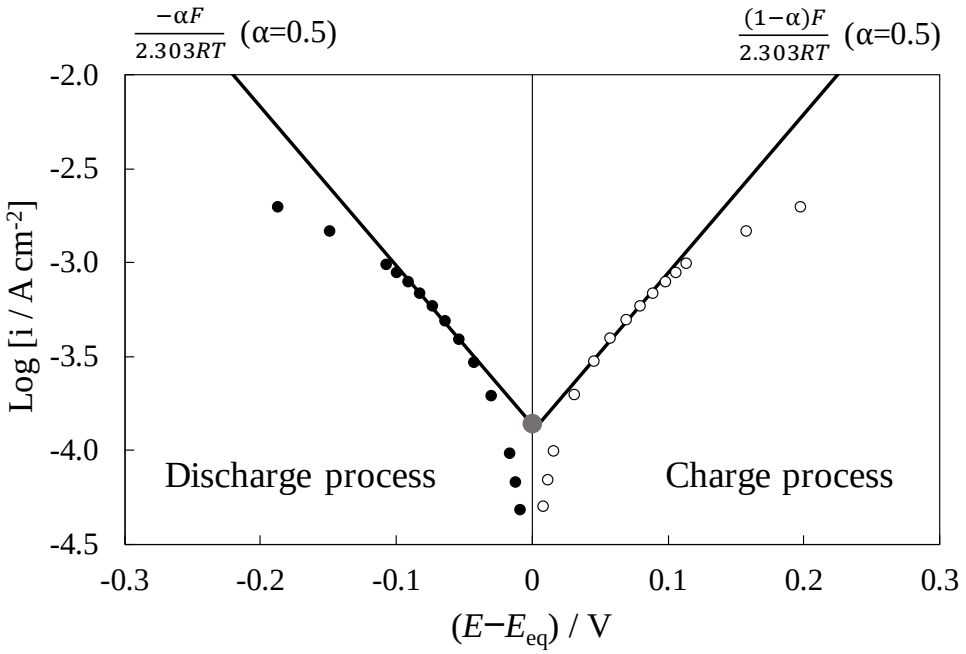

Figure 9. Quasi Tafel plots of an uncycled $LiNi_{0.8}Co_{0.15}Al_{0.05}O_2$ particle in the charge process and discharge process. α in the Tafel equation was determined 0.5 from the symmetry of the Quasi Tafel plots. After setting DOD of 10 %, a current pulse test which is repetition of “charge, rest, discharge, and rest” with various currents (0.5, 0.7, 1, 2, 3, 4, 5, 6, 7, 8, 9, 10, 15, and 20 nA) was conducted.

Table 2. Exchange current densities, charge transfer resistances, and apparent diffusion coefficients for single $LiNi_{0.8}Co_{0.15}Al_{0.05}O_2$ particle before and after cycling.

Sample	Uncycled	Cycled 400 times	Cycled 800 times
Exchange current density (i_0) [$\times 10^{-1}$ mA cm^{-2}]	1.5	0.3	0.01–0.04
Charge transfer resistance (R_{ct}) [$\times 10^{3}$ Ω cm^{2}]	0.2	0.8	6.2–33
Apparent diffusion coefficient (D) [$\times 10^{-10}$ cm^{2} s^{-1}]	2.0	1.3	< 0.2

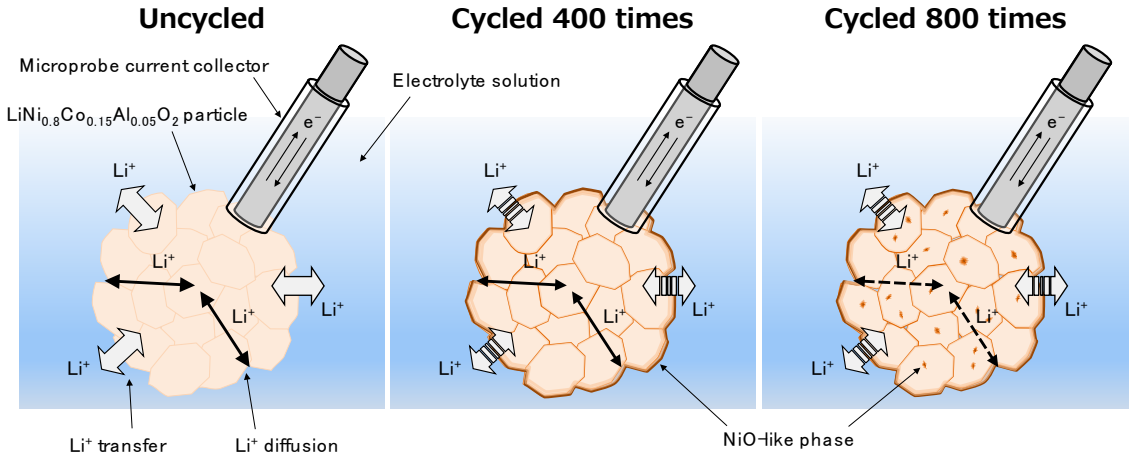

Figure 10. Schematic model of the degradation of a $LiNi_{0.8}Co_{0.15}Al_{0.05}O_2$ particle during cycling.

Chapter 5. General Conclusions

The degradation mechanism of a lithium-ion battery was examined in detail by dV/dQ curve analysis and single-particle measurement. By dV/dQ curve analysis, I efficiently investigate the relationship between test conditions and degradation factors. The consumption of lithium ions caused by the degradation of the electrolyte mainly led to the capacity fading in calendar degradation. On the other hand, at specific values of SOC and temperature, the positive electrode material also degraded considerably. Furthermore, the dV/dQ curve analysis clarified that the charged state of the electrode changes even when the storage voltage is the same due to calendar degradation. Furthermore, degradation was analyzed more quantitatively during cycle degradation. Hence, capacity fading is caused by the degradation of the positive electrode and SEI formation/growth, leading to the consumption of lithium ions, and the degree of influence varies depending on the range of temperatures and SOCs. In the single-particle measurement, the electrochemical parameters of the positive electrode-active material, the structural change of which was observed during the cycle degradation, were successfully evaluated. The structural change of the outermost particle surface of the layered materials occurred because of the cycle, followed by the

structural change of the particle inside. These step changes first led to the decrease in the exchange current density first decreases and then the diffusion coefficient.

By the application of these analysis to various batteries and active materials, the composition of the lithium-ion battery with no degradation can be clarified, as well as usage conditions with no degradation.

List of Publications

Calendar Degradation Mechanism of Lithium-Ion Batteries with a $LiMn_2O_4$ and $LiNi_{0.5}Co_{0.2}Mn_{0.3}O_2$ Blended Cathode

Keisuke Ando, Tomoyuki Matsuda, Masao Myojin, Daichi Imamura

ECS Transactions, 75 (2017) 77–90.

Degradation Diagnosis of Lithium-Ion Batteries with a $LiNi_{0.5}Co_{0.2}Mn_{0.3}O_2$ and $LiMn_2O_4$ Blended Cathode Using dV/dQ Curve Analysis

Keisuke Ando, Tomoyuki Matsuda, Daichi Imamura

Journal of Power Sources, 390 (2018) 278–285.

Degradation Analysis of $LiNi_{0.8}Co_{0.15}Al_{0.05}O_2$ for Cathode Material of Lithium-Ion Battery Using Single Particle Measurement

Keisuke Ando, Yuto Yamada, Kei Nishikawa, Tomoyuki Matsuda, Daichi Imamura, Kiyoshi Kanamura

ACS Applied Energy Materials, in press.

Acknowledgements

These experiments were partially supported by the New Energy and Industrial Technology Development Organization (NEDO), the New Energy Promotion Council (NEPC), and JSPS KAKENHI Grant Number JP15K17928, and partially conducted at the Global Research Center for Environment and Energy based on Nanomaterials Science (GREEN).

These experiments have been carried out under the supervision of Professor Kiyoshi Kanamura at Department of Applied Chemistry, Graduate School of Urban Environmental Sciences, Tokyo Metropolitan University. I would like to express my heartfelt appreciation to Prof. Kiyoshi Kanamura for his valuable advice and kind supervision.

I would like to express my sincere gratitude to Professor Katsumi Uchiyama, and Associate Professor Koichi Kajihara at Department of Applied Chemistry, Graduate School of Urban Environmental Sciences, Tokyo Metropolitan University, for their helpful comments.

I would like to extend my appreciation to Dr. Yuto Yamada at Tokyo Metropolitan University, and Dr. Kei Nishikawa at National Institute for Materials Science for their valuable advices.

I am grateful to Dr. Daichi Imamura, Dr. Tomoyuki Matsuda, Mr. Masao Myojin, Dr. Yoshiyuki Hashimasa, Dr. Motoaki Akai, Dr. Eiji Kuroda, and other members related to Japan Automobile Research Institute for their helpful advice and support.

I would like to thank to Assistant Professor Hirokazu Munakata, Mr. Masao Seki, Dr. Mao Shoji, Dr. Jungo Wakasugi, Dr. Yuta Maeyoshi, Mr. Tomohiro Omura, Mr. Masashi Konya, Mr. Takuya Kanbara, Dr. Hiroki Yamashita, Ms. Motoko Nagasaki, and other members associated with Kanamura Laboratory at Tokyo Metropolitan University, and Mr. Keisuke Shinoda at National Institute for Materials Science for their support.

Finally, I want to thank my mother, Chikako Ando for her warmth and encouragement. I would like to extend my deepest gratitude to my late father, Tsutomu Ando. I am forever thankful to him for everything.